

# A neural optimization framework for free-boundary diffeomorphic mapping problems and its applications

Zhehao Xu · Lok Ming Lui

Received: date / Accepted: date

**Abstract** Free-boundary diffeomorphism optimization is a core ingredient in the surface mapping problem but remains notoriously difficult because the boundary is unconstrained and local bijectivity must be preserved under large deformation. Numerical Least-Squares Quasiconformal (LSQC) theory, with its provable existence, uniqueness, similarity-invariance and resolution-independence, offers an elegant mathematical remedy. However, the conventional numerical algorithm requires landmark conditioning, and cannot be applied into gradient-based optimization. We propose a neural surrogate, the Spectral Beltrami Network (SBN), that embeds LSQC energy into a multiscale mesh-spectral architecture. Next, we propose the SBN guided optimization framework SBN-Opt which optimizes free-boundary diffeomorphism for the problem, with local geometric distortion explicitly controllable. Extensive experiments on density-equalizing maps and inconsistent surface registration demonstrate our SBN-Opt's superiority over traditional numerical algorithms.

**Keywords** Quasiconformal geometry · Free-boundary diffeomorphism problem · Surface registration · Deep Learning

**Mathematics Subject Classification (2020)** 30C62 · 65D18 · 65K10 · 68T07

## 1 Introduction

Diffeomorphic mappings are indispensable in computational geometry and medical imaging because they register surfaces while exactly preserving topol-

---

Zhehao Xu  
Department of Mathematics, The Chinese University of Hong Kong, Hong Kong, China  
E-mail: zhxu@math.cuhk.edu.hk

Lok Ming Lui  
Department of Mathematics, The Chinese University of Hong Kong, Hong Kong, China  
E-mail: lmlui@math.cuhk.edu.hk

ogy. Practical examples abound: population cartograms rescale countries to equalize density [9, 29]; surgeons “unfold” the cerebral cortex to a flat view for easier navigation [5]; and manufacturers flatten curved sheets to design cutting patterns for free-form parts [33]. In each case, the task is to map a given surface to the plane. Crucially, the shape of the planar image is often unknown in advance. The algorithm must infer the boundary shape so that the final map captures target properties such as area distribution, curvature, or feature alignment. We refer to this setting as the free-boundary diffeomorphism problem.

Established works like [11] provide efficient algorithms for computing a conformal disk parameterization of an open surface, hence mathematically, the problem can be formulated as finding an optimal mapping on the unit disk  $\mathbb{D}$  such that

$$f = \operatorname{argmin}_{g: \mathbb{D} \rightarrow \mathbb{C}} E(g) \text{ subject to } g \in \mathcal{C}, \quad (1)$$

where  $E$  is a mapping energy functional and  $\mathcal{C}$  denotes the admissible maps. Because practical applications demand bijectivity, we choose  $\mathcal{C}$  as the space of diffeomorphisms.

The diffeomorphism optimization problem is generally challenging due to the nonlinearity and complexity of the constraint space. In the context of a fixed target domain, numerous effective methods have been developed for computing diffeomorphisms, each contributing valuable advancements to the field. For instance, flow-based techniques including LDDMM [20] and SVF [2], offer a principled way to generate diffeomorphisms by solving ordinary differential equations, which enables handling complex scenarios like large deformations. Other methods including [13, 22, 29, 30, 36, 38], have also shown impressive results in practice. Nevertheless, each approach contains inherent trade-offs. For instance, flow-based strategies require solving an ODE to obtain the diffeomorphism, which can become computationally intensive, especially for high-resolution data. Some alternative methods rely on carefully tuning the optimization step size [29, 30, 36] or post hoc projection [22] to prevent local fold-over, or they introduce barrier energy terms [13, 38] to reduce the risk of folding. While such modifications are effective in many cases, they may not always guarantee bijectivity, and their effectiveness can depend sensitively on parameter choices and problem context.

Moreover, in a free-boundary diffeomorphism optimization problem, the shape of the target domain is not known in advance and typically depends on the optimization objective. This makes the problem significantly more challenging: the solver must simultaneously determine both the mapping and the geometry of the target domain. To address this challenge, most prior methods introduce additional constraints, such as fixing the positions of certain landmark points, adding artificial boundary frames, or prescribing a fixed outer boundary shape to anchor the solution and prevent degenerate outcomes [9, 35]. At the same time, many applications also require bounded geometric distortion. Balancing injectivity, distortion control, and optimizing target geometry produces a highly nonconvex optimization landscape, where algorithms can easily become trapped in undesirable, suboptimal solutions.

Therefore, our focus is developing a method for computing free-boundary diffeomorphisms, which has theoretic guarantee for bijectivity and can more efficiently control the local geometric distortion. To remove the need for boundary scaffolds while explicitly controlling local distortion, we recast the task as minimizing the least squares quasiconformal (LSQC) energy [34]

$$E_{\text{LSQC}}(f, \mu) = \frac{1}{2} \int_{\mathbb{D}} \|f_{\bar{z}} - \mu f_z\|^2 dA.$$

As validated in Sec.5, numerical implementation of LSQC enjoys properties including existence and uniqueness of the minimizer, invariance due to a similarity transformation, and independence of mesh resolution. However, differentiating through the classical LSQC solver is computationally expensive, which limits its use in gradient-based optimization pipelines. To overcome this, we develop the **Spectral Beltrami Network (SBN)**, a deep neural network designed to act as a neural surrogate for the LSQC solver that approximates the LSQC solution in a single fully differentiable forward pass. Given Beltrami coefficients  $\mu$  (BCs) on the disk, SBN predicts a map that closely matches the output of the numerical solver without prescribing any boundary information. After the training of SBN stops, we freeze the parameters of SBN and treat BCs  $\mu$  as the explicit, trainable input to SBN, shifting the optimization problem from searching directly in the unstable space of vertex coordinates to a well-structured space of BCs  $\{\mu : \|\mu\|_{\infty} < 1\}$  which essentially is the space of diffeomorphisms by the quasiconformal theory [14].

Within this, we propose a novel framework for the free-boundary diffeomorphism problem which solves the problem 1 by

$$\min_{(\mu_v, p_i, \phi, s, r)} E_1 \left( g(\mathcal{F}_{\theta^*}(\mu_v, p_1, p_2), \phi, s, r) \right) + E_2(\mu) \quad (2)$$

where  $\mathcal{F}_{\theta^*}$  is the SBN,  $g$  is the similarity transformation that  $g(x, \phi, s, r) = se^{i\phi}x + r$ ,  $E_1$  and  $E_2$  are energy functionals on the mapping and BCs, respectively. Since the key component of the framework is SBN, we abbreviate the framework to **SBN-Opt**. The SBN-Opt changes from 'optimization over all deformations' to 'optimization over diffeomorphisms', giving us explicit, mathematically guaranteed control over both boundary freedom and local geometric distortion while maintaining the efficiency of a single forward pass.

The rest of the paper is organized as follows. Sec.2 reviews previous works related to our proposed framework. Sec.3 lists the contributions of this paper. Sec.4 introduces the mathematical theories involved in our work. In Sec.5 we propose and prove several key properties of LSQC energy. Then we introduce the architecture of Spectral Beltrami Network in Sec.6 and the optimization framework SBN-Opt in Sec.7 followed by implementation details in Sec.8 and extensive experiments in Sec.9. Lastly, a conclusion is given in Sec.10.

## 2 Previous works

Our research objective is to develop an efficient algorithm for the free-boundary diffeomorphism optimization problem, which can explicitly control the local geometric distortion. Therefore, we may review some representative works on the diffeomorphism optimization problem. Besides, since our strategy involves the quasiconformal theory, previous works related to computational quasiconformal geometry are also discussed in this section. Below we give a focused but not exhaustive overview of the most relevant prior works.

### 2.1 Diffeomorphism Optimization Problem

Diffeomorphic mapping provides one-to-one as well as smooth correspondences across different objects of interest, which serves as a powerful registration tool and has been successfully applied to many scenarios including image segmentation and image registration. Numerous works have been proposed for this problem. For example, the Large Diffeomorphic Distance Metric Mapping (LDDMM) [20] maps the template domain onto the target one by defining and solving an ordinary differential equation (ODE). Stationary Vector Field (SVF) [2] is also defined by an ODE but different from LDDMM with time-varying speed flows, SVF provides stationary-speed vector fields and obtains the flow via exponential of the vector field. Later methods like DARTEL [3] and diffeomorphic Demons [40] further accelerate registration by exploiting Lie-algebra parameterizations, yet they still depend on careful regularization to avoid foldovers near steep deformations. To enforce injectivity more directly, barrier-energy terms [13, 38] that penalize near-zero Jacobian determinants and projection schemes [22] that iteratively map invalid solutions back into the admissible set have been introduced, trading simplicity for additional optimization complexity and still only providing indirect control of distortion. Recent learning-based approaches [1, 23, 41] predict velocity fields or full deformations in one forward pass, replacing costly iterative solvers, yet most did not involve control over local geometric distortion.

When comes to a free-boundary setting, achieving rigorous invertibility and tight distortion control without relying on boundary scaffolds or handcrafted regularizers remains challenging. One stream of methods is treating boundary points as individual optimization parameters and updating them in an iterative nonlinear numerical scheme. For example, Smith and Schaefer [38] designed a barrier distance function to avoid intersection of boundary edges. Another direction is to determine the boundary via the desired geometric properties in the inner region and geometry of the original surface. A typical work is the least squares conformal maps (LSCM) [24], which obtain a free-boundary conformal parameterization of a surface via solving a linear system. An alternative 'sea-padding' strategy [9] embeds the domain inside a large auxiliary rectangle whose rigid outer edge serves as an implicit boundary.



## 2.2 Computational Quasiconformal Geometry

Since the seminal introduction of discrete conformal mapping to computer graphics [15, 16, 19, 21], conformal techniques have become indispensable for surface processing. Lui and collaborators extended this framework to quasiconformal registration, developing the Linear Beltrami Solver (LBS) [27], which accommodates large deformations, guarantees bijectivity, and proved effective in medical imaging and surface matching [10, 28–30]. However, it still requires explicit boundary point correspondences. Drawing inspiration from LSCM [24], Qiu and Lui introduced the least squares quasiconformal (LSQC) energy [34], removing the need for prescribed boundary constraints and thus broadening applicability to tasks such as inconsistent surface registration [8, 35] and partial welding [42]. This boundary-free formulation underpins our work. More recently, several studies [7, 17] have coupled the quasiconformal theory with deep learning, training neural networks to map Beltrami coefficients to diffeomorphisms but these efforts simulate LBS within a fixed domain. Our Spectral Beltrami Network demonstrates, for the first time, that a neural surrogate can faithfully approximate the free-boundary LSQC solution, combining the advantage of deep learning with the theoretical guarantees of quasiconformal geometry.

## 3 Contributions

Our work has several key contributions and novel aspects to the field of free-boundary diffeomorphism optimization problem. Specifically, our contributions are as follows:

1. Several crucial properties of LSQC are proven, including existence and uniqueness, exact satisfaction of the Beltrami equation, guarantee of reconstructing diffeomorphism, invariance under similarity transformations, and resolution independence. These theoretical guarantees provide a solid mathematical foundation that enables its application to free-boundary diffeomorphism optimization.
2. A novel neural network architecture Spectral Beltrami Network (SBN) is designed to simulate LSQC, which innovatively combines:
  - **Multiscale message-passing mechanisms** that enable efficient information exchange across different mesh resolutions
  - **Mesh Spectral Layers (MSL)** that leverage Laplacian eigenmodes to capture global geometric dependencies

As a differentiable surrogate of LSQC, SBN can compute free-boundary quasiconformal mappings on the unit disk, given Beltrami coefficients and two pinned points.

3. We established SBN-Opt, a novel optimization framework that uses the SBN as a differentiable engine to solve complex free-boundary diffeomorphism problems. Instead of merely training a network for one-shot predictions, SBN-Opt establishes a complete gradient-based optimization loop over the

space of admissible BCs, equivalently the space of diffeomorphisms. Key features include:

- **Direct Optimization over Geometric Priors:** The framework enables direct, gradient-based optimization of the underlying BCs  $\mu$ . This allows for explicit and intuitive control over local geometric properties like angle distortion.
- **Free of landmark conditions:** Different from the traditional optimization scheme using the numerical LSQC algorithm which is landmark-dependent, SBN-Opt is designed to solve the optimization problem by simultaneously optimizing BCs and two pinned points thus is more flexible and able to applied to general free-boundary diffeomorphism problems.

This framework effectively bridges the gap between the theoretical guarantees of quasiconformal geometry and the practical flexibility of deep learning, creating a powerful new tool for surface registration and parameterization.

## 4 Mathematical Background

### 4.1 Quasiconformal Mappings

Quasiconformal mappings generalize conformal mappings by extending orientation-preserving homeomorphisms to those with bounded conformality distortions. Mathematically, suppose  $\Omega$  is a domain in  $\mathbb{C}$ , a mapping  $f: \Omega \rightarrow \mathbb{C}$  is a quasi-conformal map if it satisfies the Beltrami equation

$$\frac{\partial f}{\partial \bar{z}} = \mu(z) \frac{\partial f}{\partial z} \quad (3)$$

for some measurable complex-valued function  $\mu$  with  $\|\mu\|_\infty < 1$ , where  $\frac{\partial f}{\partial \bar{z}} = \frac{1}{2}(f_x - if_y)$  and  $\frac{\partial f}{\partial z} = \frac{1}{2}(f_x + if_y)$ .  $\mu$  is called the complex dilation or Beltrami coefficient (BC) of  $f$ , which measures the local deviation from a conformal map.

Let  $f: (x, y) \rightarrow (u, v)$  and  $\mu = \rho + i\tau$ , and denote by  $\mathbf{S}(2)$  the space of all  $2 \times 2$  symmetric positive definite matrices whose determinant is 1, then

$$D_f(z)^T D_f(z) = |\det D_f(z)| Q(z) \quad (4)$$

where  $Q = (Q_{ij}): \Omega \rightarrow \mathbf{S}(2)$ . Right multiplying both sides by  $D_f(z)^{-1}$ , we obtain a linear system which is the alternative formulation of the Beltrami equation:

$$\begin{bmatrix} u_x & u_y \\ v_x & v_y \end{bmatrix}^T = \text{sgn}(J_f(x)) \cdot \begin{bmatrix} q_{11} & q_{12} \\ q_{12} & q_{22} \end{bmatrix} \begin{bmatrix} v_y & -u_y \\ -v_x & u_x \end{bmatrix}, \quad (5)$$

and from this we have  $\mu = \frac{q_{11} - q_{22} + 2iq_{12}}{q_{11} + q_{22} + 2\text{sgn}(\det D_f)}$ . With the constraint that  $Q(z) \in \mathbf{S}(2)$ , we observe that  $|\mu(z)| < 1$  if and only if  $\det D_f(z) > 0$ . By inverse function theorem, researchers would through restricting  $\|\mu\|_\infty < 1$ , achieve local bijectivity and prevent folding in the triangular mesh [10, 28].

Suppose  $\mu(z)$  is a measurable complex-valued function defined in a domain  $U \subseteq \mathbb{C}$  for which  $\|\mu\|_\infty < 1$ , we have the following existence theorem.

**Theorem 1 (Measurable Riemann Mapping Theorem)** *For any function  $\mu : U \rightarrow \mathbb{C}$  on with bounded essential supremum norm  $\|\mu\|_\infty < 1$ , there is a quasiconformal map  $\phi$  on  $\bar{U}$  satisfying the Beltrami equation  $\phi_{\bar{z}} = \mu\phi_z$  for almost all  $z \in U$ . Moreover,  $\phi$  is unique up to post-composition with conformal isomorphisms and  $\phi$  depends holomorphically on  $\mu$ .*

When comes to discretization, it is a natural manner to ask whether there is a numerical method to compute the quasiconformal mapping given the BCs. The answer is yes, thanks to the Least Squares Quasiconformal Energy.

## 4.2 Least Squares Quasiconformal Energy

Apart from Eq.5, the Beltrami equation can be rewritten as

$$\begin{bmatrix} v_y \\ -v_x \end{bmatrix} = \frac{1}{1 - |\mu|^2} \begin{bmatrix} (\rho - 1)^2 + \tau^2 & -2\tau \\ -2\tau & (1 + \rho)^2 + \tau^2 \end{bmatrix} \begin{bmatrix} u_x \\ u_y \end{bmatrix}. \quad (6)$$

Here we assume  $|\mu| < 1$  and for convenience, we denote the square matrix on the right-hand side by  $\mathbf{A}$ . Inspired by the least squares conformal energy [24], Qiu [34] proposed the concept least squares quasiconformal (LSQC) energy of a map.

**Definition 1** Let  $\mu = \rho + ir$  be a complex-valued function defined on the domain  $\Omega$ . The LSQC energy of the map  $z = (x, y) \mapsto (u, v)$  against the BC  $\mu$  is defined to be

$$E_{LSQC}(u, v, \mu) = \frac{1}{2} \int_{\Omega} \|P\nabla u + JP\nabla v\|^2 dx dy, \quad (7)$$

where

$$P = \frac{1}{\sqrt{1 - |\mu|^2}} \begin{bmatrix} 1 - \rho & -r \\ -r & 1 + \rho \end{bmatrix}, J = \begin{bmatrix} 0 & -1 \\ 1 & 0 \end{bmatrix},$$

so that  $P^T P = \mathbf{A}$  as in Eq.6 and  $P^T J P = J$ .

The LSQC energy admits the decomposition

$$E_{LSQC}(u, v, \mu) = E_{\mathbf{A}}(u; \Omega) + E_{\mathbf{A}}(v; \Omega) - \mathcal{A}(u, v) \quad (8)$$

where

$$E_{\mathbf{A}}(u; \Omega) = \frac{1}{2} \int_{\Omega} \nabla u^T \mathbf{A} \nabla u dx dy = \frac{1}{2} \int_{\Omega} \|P\nabla u\|^2 dx dy$$

is the Dirichlet-type energies of second-order equation  $\nabla \cdot (\mathbf{A} \nabla u(z)) = 0$  derived by the decoupling method [28] and

$$\mathcal{A}(u, v) = \int_{\Omega} (u_y v_x - u_x v_y) dx dy. \quad (9)$$

is the area of the image.

Given a piecewise linear map  $f(x, y) = u + \sqrt{-1}v$  and consider a triangle  $T = (x_j, y_j)_{j=1,2,3}$  of  $\mathbb{R}^2$ , we have

$$\begin{pmatrix} \partial u / \partial x \\ \partial u / \partial y \end{pmatrix} = \frac{1}{d_T} \begin{pmatrix} y_2 - y_3 & y_3 - y_1 & y_1 - y_2 \\ x_3 - x_2 & x_2 - x_1 & x_1 - x_2 \end{pmatrix} \begin{pmatrix} u_1 \\ u_2 \\ u_3 \end{pmatrix}$$

where  $d_T = (x_1 y_2 - y_1 x_2) + (x_2 y_3 - y_2 x_3) + (x_3 y_1 - y_3 x_1)$  is twice the area of the triangle. The Beltrami equation (Eq.3) can be rewritten as  $(1 - \mu)f_x + i(1 + \mu)f_y = 0$  and collected as a complex-valued linear system.

$$0 = \frac{i}{d_T} (W_1 \quad W_2 \quad W_3) (U_1 \quad U_2 \quad U_3)^\top$$

where  $U_j = u_j + \sqrt{-1}v_j$  and

$$\begin{aligned} W_1 &= (1 + \mu)(x_3 - x_2) + \sqrt{-1}(1 - \mu)(y_3 - y_2) \\ W_2 &= (1 + \mu)(x_1 - x_3) + \sqrt{-1}(1 - \mu)(y_1 - y_3) \\ W_3 &= (1 + \mu)(x_2 - x_1) + \sqrt{-1}(1 - \mu)(y_2 - y_1). \end{aligned}$$

As a result,

$$\begin{aligned} E_{LSQC}(\mathbf{U} = (U_1, \dots, U_{|\mathcal{V}|})) &= \sum_{T \in \mathcal{T}} d_T \left| ((1 - \mu)f_x + i(1 + \mu)f_y) \Big|_T \right|^2 \\ &= \sum_{T \in \mathcal{T}} \frac{1}{d_T} \left| (W_{1,T} \quad W_{2,T} \quad W_{3,T}) (U_{1,T} \quad U_{2,T} \quad U_{3,T})^\top \right|^2 \end{aligned}$$

and we may write as  $E_{LSQC}(\mathbf{U}) = \|\mathcal{M}\mathbf{U}\|^2$  with  $\mathcal{M} = (m_{ij}) \in \mathbb{C}^{|\mathcal{F}| \times |\mathcal{V}|}$  defined as

$$\mathcal{M}_{ij} = \begin{cases} W_{j,T_i} & \text{if } j \text{ is a vertex of the face } T_i, \\ 0 & \text{otherwise.} \end{cases}$$

To obtain a nontrivial solution, some of the  $U_i$ 's have to be pinned.

We decomposed  $\mathbf{U} = (\mathbf{U}_f^\top, \mathbf{U}_p^\top)^\top$ , where  $\mathbf{U}_f$  are free points, i.e. variables of the optimization problem, and  $\mathbf{U}_p$  are the points pinned. Similarly, we can decompose  $\mathcal{M}$  in blocked matrices as

$$\mathcal{M} = (\mathcal{M}_f, \mathcal{M}_p)$$

with  $\mathcal{M}_f \in \mathbb{C}^{|\mathcal{F}| \times (|\mathcal{V}| - p)}$  and  $\mathcal{M}_p \in \mathbb{C}^{|\mathcal{F}| \times p}$ . Let  $^1$  and  $^2$  be real and imaginary parts of a complex number, and rewrite the  $|\mathcal{F}|$  complex linear equations to  $2|\mathcal{F}|$  real equations, we have

$$E_{LSQC}(\mathbf{U}) = \|\mathcal{A}\mathbf{u} - \mathbf{b}\|^2$$

where  $\mathbf{u} = ((\mathbf{U}_f^1)^\top, (\mathbf{U}_f^2)^\top)^\top$  and

$$\mathcal{A} = \begin{pmatrix} \mathcal{M}_f^1 & -\mathcal{M}_f^2 \\ \mathcal{M}_f^2 & \mathcal{M}_f^1 \end{pmatrix}, \mathbf{b} = - \begin{pmatrix} \mathcal{M}_p^1 & -\mathcal{M}_p^2 \\ \mathcal{M}_p^2 & \mathcal{M}_p^1 \end{pmatrix} \begin{pmatrix} \mathbf{U}_p^1 \\ \mathbf{U}_p^2 \end{pmatrix}.$$

Finally, the nontrivial solution is  $\mathbf{U} = \begin{pmatrix} (\mathcal{A}^\top \mathcal{A})^{-1} \mathcal{A}^\top \mathbf{b} \\ \mathbf{U}_p \end{pmatrix}$ .

Although LSQC has been used in numerical computations, its theoretical properties and suitability for neural simulation have not been systematically studied. We address this gap in the following section.

## 5 Properties of Least Squares Quasiconformal Energy

We now analyze the properties of LSQC energy that make it uniquely suitable for computing the corresponding quasiconformal mappings.

In discretization, the numerical solution  $U$  is unique when at least two points' destinations are prescribed [34]. Here is the statement with proof.

**Proposition 1** *Suppose  $\|\mu\|_\infty < 1$ , and the triangulation mesh is connected without dangling triangles. As long as  $p \geq 2$ , then  $\mathcal{A}$  has full rank.*

*Proof* The argument is essentially same as that in [24]. The idea is that start with the pinned points, we can construct the triangular mesh  $\mathcal{T}$  incrementally via two operations:

1. glue: add a new vertex and connect it to two neighboring vertices.
2. join: connect two existing vertices.

Correspondingly, the matrix  $\mathcal{M}$  is constructed incrementally as well. Let  $\mathcal{M}^{(i)} \in \mathbb{C}^{|\mathcal{F}_i| \times |\mathcal{V}_i|}$  be the  $\mathcal{M}$  based on the constructed triangulation after  $i$ -th step. Two key observations are that  $|\mathcal{F}_i| \geq |\mathcal{V}_i| - 2$  and the rank of  $\mathcal{M}_f^{(i)}$  is always its column number. If the  $(i+1)$ -th step is a joining operation, then compared to  $\mathcal{M}_f^{(i)}$ ,  $\mathcal{M}_f^{(i+1)}$  just has one more row, and joining has no affect on the rank. If the  $(i+1)$ -th step is a gluing operation, then  $\mathcal{M}_f^{(i+1)}$  has one more row and column, and the new column has only one nonzero element in the last row thus the rank still equals to the column number. The premise of the argument is that for each triangle  $T$ , correspond  $W_{j,T}$  are nonzero. This is still true when  $\|\mu\|_\infty < 1$ . Let  $\mu = \rho + \sqrt{-1}\tau$  and  $L = \begin{pmatrix} 1 + \rho & \tau \\ \tau & 1 - \rho \end{pmatrix}$ , then  $W_{j,T} = (1 \ \sqrt{-1}) L \begin{pmatrix} x_{j+2} - x_{j+1} \\ y_{j+2} - y_{j+1} \end{pmatrix}$ . Since  $\|\mu\|_\infty < 1$  and  $\mathcal{T}$  is a non-degenerate triangulation, then  $L$  is non-singular and  $W_{j,T}$  are all nonzero. Last, since  $\mathcal{M}_f$  is a full-rank complex matrix,  $\mathcal{A}$  also has full rank.

A natural corollary is the existence and uniqueness of minimizer of LSQC energy with  $p \geq 2$  points pinned, given by  $\mathbf{x} = (\mathcal{A}^\top \mathcal{A})^{-1} \mathcal{A}^\top \mathbf{b}$ . On the other hand, pinning too many points would overdetermine the system and the solution may not be compatible with the provided BCs. Therefore, it is preferred to only pin two points that are far from each other to avoid an unnatural local scale change. Consequently, if  $|\mathcal{F}| = |\mathcal{V}| - 2$  the numerical result  $\mathbf{U}$  is an analytic solution to the Beltrami equation, provided face-wise constant  $\mu$ .

**Corollary 1** Suppose  $\|\mu\|_\infty < 1$  and face-wise constant, and  $\mathbf{U}$  is the face-wise linear solution by solving the LSQC system with two points pinned. If  $|\mathcal{F}| = |\mathcal{V}| - 2$ , then the BC for each face, induced by  $\mathbf{U}$ , is exactly the provided  $\mu$ .

*Proof* Since the number of pinned points is 2 and no triangle face is predetermined,  $\mathcal{M}_f$  has exactly  $|\mathcal{F}| = |\mathcal{V}| - 2$ , equal to the number of columns. By above, we know  $\mathcal{M}_f$  has full rank and thus  $\mathcal{A}$  is an invertible square matrix. Therefore,  $\mathbf{U} = \mathcal{A}^{-1}\mathbf{b}$  and  $E_{\text{LSQC}}(\mathbf{U}) = 0$ . Consequently, let  $\mathbf{U} = u + \sqrt{-1}v$ , then  $P\nabla u + JP\nabla v = 0$  on each face.

However, it is more common that the LSQC energy functional of a given BC does not have a zero-value minimizer, because there is inherently no face-wise linear homeomorphism for the given face-wise constant BC or  $|\mathcal{F}| \neq |\mathcal{V}| - 2$ . Despite this, once the provided face-wise constant BC is induced by a face-wise linear homeomorphism, the LSQC algorithm can reconstruct the homeomorphism given the induced BC and two points of the homeomorphism.

**Corollary 2** Suppose  $\mathcal{T}$  is a triangular mesh,  $F$  is a face-wise linear homeomorphism of  $\mathcal{T}$  and  $F(p_1) = q_1, F(p_2) = q_2$ , let  $\mu$  be the face-wise constant BC induced by  $F$ , then the solution of the LSQC system derived by  $\mu$  and pinning  $F(p_1) = q_1, F(p_2) = q_2$  is exactly the  $F$ .

*Proof* With two points pinned, the LSQC system has only one minimizer satisfying the pin-point condition. Since  $\mu$  is induced by  $F$ ,  $P\nabla u + JP\nabla v = 0$  on each face and  $E_{\text{LSQC}}(F) = 0$ . Meanwhile,  $F$  satisfies the pin-point condition, and thus it is the solution to the LSQC system.

In addition, the solution is invariant by a similarity transformation, which fits the implication of the composition formula  $\mu_{g \circ f} = \frac{\mu_f + \overline{f_z}/f_z(\mu_g \circ f)}{1 + \overline{f_z}/f_z \overline{\mu_f}(\mu_g \circ f)}$  that post-composition of a conformal mapping  $g$  does not change the BCs of the original function  $f$ .

**Proposition 2** Given  $\mu$  and pinned points  $\mathbf{U}_p$  and denote the corresponding free-point solution by  $\mathbf{U}_f$ , if the pinned points are transformed to  $z\mathbf{U}_p + \mathbf{T}$  where  $z \in \mathbb{C}, \mathbf{T} = (z', \dots, z')^\top \in \mathbb{C}^{|\mathcal{V}|}$ , then the corresponding free-point solution is  $z\mathbf{U}_f + \mathbf{T}$ .

*Proof* If  $z = e^{i\theta}$  with  $\theta \in \mathbb{R}$ , then

$$\begin{aligned} \min_{\tilde{\mathbf{U}}} E_{\text{LSQC}}(\tilde{\mathbf{U}}, \mathbf{U}_p) &= E_{\text{LSQC}}(\mathbf{U}_f, \mathbf{U}_p) = (\mathcal{M}\mathbf{U})^* \mathcal{M}\mathbf{U} \\ &= z^* z (\mathcal{M}\mathbf{U})^* \mathcal{M}\mathbf{U} = E_{\text{LSQC}}(z\mathbf{U}_f, z\mathbf{U}_p) \\ &\geq \min_{\tilde{\mathbf{U}}} E_{\text{LSQC}}(\tilde{\mathbf{U}}, z\mathbf{U}_p) \end{aligned}$$

On the other hand, denote the  $\arg\min_{\tilde{\mathbf{U}}} E_{\text{LSQC}}(\tilde{\mathbf{U}}, z\mathbf{U}_p)$  by  $\hat{\mathbf{U}}_f$ , we have

$$\min_{\tilde{\mathbf{U}}} E_{\text{LSQC}}(\tilde{\mathbf{U}}, z\mathbf{U}_p) = E_{\text{LSQC}}(z^* \hat{\mathbf{U}}_f, \mathbf{U}_p) \geq \min_{\tilde{\mathbf{U}}} E_{\text{LSQC}}(\tilde{\mathbf{U}}, \mathbf{U}_p)$$

Therefore,  $\min_{\tilde{\mathbf{U}}} E_{\text{LSQC}}(\tilde{\mathbf{U}}, \mathbf{U}_p) = \min_{\tilde{\mathbf{U}}} E_{\text{LSQC}}(\tilde{\mathbf{U}}, z\mathbf{U}_p)$  and  $\hat{\mathbf{U}}_f = z\mathbf{U}_f$ . If  $z \in \mathbb{R}$ , then the minimizer is  $(\mathcal{A}^\top \mathcal{A})^{-1} \mathcal{A}^\top (z\mathbf{b}) = z(\mathcal{A}^\top \mathcal{A})^{-1} \mathcal{A}^\top \mathbf{b} = z\mathbf{U}_f$ . Lastly, the invariance by a translation is followed by the observation that  $\sum_{i=1}^3 w_{i,T} = 0$  and  $(1, 1, \dots, 1)^\top \in \ker \mathcal{M}$ .

In all, LSQC also has its own properties related to solution's uniqueness and existence given points pinned, as well as invariant by a family of transformations, which is very analogous to Thm.1. Moreover, the solution of the minimization problem is independent of the resolution of the mesh.

**Proposition 3** *Suppose we have a triangulation  $\mathcal{T} = (\mathcal{V}, \mathcal{F})$  with face-wise constant  $\mu = \{\mu_T : T \in \mathcal{F}\}$ , and pinned points  $\mathbf{U}_p$ , and denote the corresponding solution by  $\mathbf{U} = (\mathbf{U}_f, \mathbf{U}_p)$ . Let  $T = (\mathbf{v}_1, \mathbf{v}_2, \mathbf{v}_3)$  be a face in  $\mathcal{T}$  and we split  $T$  into three triangles with  $\mathbf{v} = \sum_{i=1}^3 \alpha_i \mathbf{v}_i$  ( $\alpha_i > 0$ ) being the introduced vertex and  $T_i$  being the new triangles not containing  $\mathbf{v}_i$  as vertex. If  $\mu_{T_i} = \mu_T$  ( $i = 1, 2, 3$ ) and BCs on other faces remain, then the minimizer of this new minimization problem is  $\mathbf{U}^+ = (\mathbf{U}^\top, \mathbf{U}_v)^\top$  where  $\mathbf{U}_v = \sum_{i=1}^3 \alpha_i \mathbf{U}_i$ .*

*Proof* There are four cases that  $n$  ( $n = 0, 1, 2, 3$ ) of 3 vertices in  $T$  are pinned points. The case that  $n = 3$  is trivial and let's first look into the case that  $n = 0$ . In this case, inserting  $v$  would augment  $\mathcal{M}_f$  by two rows and one columns (one triangle become three triangles and add one more free point), and augment  $\mathcal{M}_p$  by one null row. Denote the new blocked matrices by  $\mathcal{M}_f^+$  and  $\mathcal{M}_p^+$ , and structure of these four matrices are: .

$$\mathcal{M}_f = \begin{pmatrix} \mathcal{N}_f \\ - \mathcal{F} - \end{pmatrix}, \mathcal{M}_f^+ = \begin{pmatrix} 0 \\ \mathcal{N}_f \\ \vdots \\ 0 \\ - \mathcal{L} - \mathcal{P} - \end{pmatrix}, \mathcal{M}_p = \begin{pmatrix} \mathcal{N}_p \\ - \mathbf{0} - \end{pmatrix}, \mathcal{M}_p^+ = \begin{pmatrix} \mathcal{N}_p \\ - \mathbf{0} - \\ \mathbf{0} \\ \mathbf{0} \end{pmatrix},$$

where  $\mathcal{N}_f \in \mathbb{C}^{(|\mathcal{F}|-1) \times (|\mathcal{V}|-p)}$ ,  $\mathcal{N}_p \in \mathbb{C}^{(|\mathcal{F}|-1) \times p}$ ,  $\mathcal{F} \in \mathbb{C}^{1 \times (|\mathcal{V}|-p)}$  with three nonzero elements  $f_j = W_{j,T}/\sqrt{d_T}$ ,  $\mathcal{L}$  and  $\mathcal{P}$  both have three rows with nonzero elements defined as:

$$l_{ij} = w_{j,T_i} = \frac{1}{\sqrt{\alpha_i}}(\alpha_i f_j - \alpha_j f_i), \quad p_i = \frac{f_i}{\sqrt{\alpha_i}}.$$

Since  $\mathbf{U}_f = -(\mathcal{M}_f^* \mathcal{M}_f)^{-1} \mathcal{M}_f^* \mathcal{M}_p \mathbf{U}_p$ , we have

$$\mathcal{M}_f^* \mathcal{M}_f \mathbf{U}_f = (\mathcal{N}_f^* \mathcal{F}^*) \begin{pmatrix} \mathcal{N}_f \mathbf{U}_f \\ \sum_{j=1}^3 f_j \mathbf{U}_j \end{pmatrix} = \mathcal{N}_f^* \mathcal{N}_f \mathbf{U}_f + (\sum_{j=1}^3 f_j \mathbf{U}_j) \mathcal{F}^* = -\mathcal{M}_f^* \mathcal{M}_p \mathbf{U}_p.$$

To prove the statement, we need to show  $\mathcal{M}_f^{+*} \mathcal{M}_f^+ \begin{pmatrix} \mathbf{U}_f \\ \mathbf{U}_v \end{pmatrix} = -\mathcal{M}_f^{+*} \mathcal{M}_p^+ \mathbf{U}_p$ .

And for the left hand side,

$$\begin{aligned} \mathcal{M}_f^{+*} \mathcal{M}_f^+ \begin{pmatrix} \mathbf{U}_f \\ \mathbf{U}_v \end{pmatrix} &= \mathcal{M}_f^{+*} \begin{pmatrix} \mathcal{N}_f \mathbf{U}_f \\ \mathcal{L} \mathbf{U}_f + (\sum_i \alpha_i \mathbf{U}_i) \mathcal{P} \end{pmatrix} = \mathcal{M}_f^{+*} \begin{pmatrix} \mathcal{N}_f \mathbf{U}_f \\ \sqrt{\alpha_1} \sum_i f_i \mathbf{U}_i \\ \sqrt{\alpha_2} \sum_i f_i \mathbf{U}_i \\ \sqrt{\alpha_3} \sum_i f_i \mathbf{U}_i \end{pmatrix} \\ &= \begin{pmatrix} \mathcal{N}_f^* \mathcal{N}_f \mathbf{U}_f \\ 0 \end{pmatrix} + \begin{pmatrix} \mathcal{L}^* \\ \mathcal{P}^* \end{pmatrix} \begin{pmatrix} \sqrt{\alpha_1} \sum_i f_i \mathbf{U}_i \\ \sqrt{\alpha_2} \sum_i f_i \mathbf{U}_i \\ \sqrt{\alpha_3} \sum_i f_i \mathbf{U}_i \end{pmatrix} \end{aligned}$$

and  $\mathcal{M}_f^{+*} \mathcal{M}_p^+ \mathbf{U}_p = \begin{pmatrix} \mathcal{M}_f^* \mathcal{M}_p \mathbf{U}_p \\ 0 \end{pmatrix}$ . So, we are left to prove

$$\begin{pmatrix} \mathcal{L}^* \\ \mathcal{P}^* \end{pmatrix} \begin{pmatrix} \sqrt{\alpha_1} \sum_i f_i \mathbf{U}_i \\ \sqrt{\alpha_2} \sum_i f_i \mathbf{U}_i \\ \sqrt{\alpha_3} \sum_i f_i \mathbf{U}_i \end{pmatrix} = \begin{pmatrix} (\sum_{j=1}^3 f_j \mathbf{U}_j) \mathcal{F}^* \\ 0 \end{pmatrix}.$$

For this, we have

$$\begin{aligned} \sqrt{\alpha_2} (\sum_{i=1}^3 f_i \mathbf{U}_i) l_{21}^* + \sqrt{\alpha_3} (\sum_{i=1}^3 f_i \mathbf{U}_i) l_{31}^* &= (\sum_{i=1}^3 f_i \mathbf{U}_i) (\alpha_2 f_1^* - \alpha_1 f_2^* + \alpha_3 f_1^* - \alpha_1 f_3^*) \\ &= (\sum_{i=1}^3 f_i \mathbf{U}_i) (\alpha_2 f_1^* + \alpha_3 f_1^* + \alpha_1 f_1^*) = (\sum_{i=1}^3 f_i \mathbf{U}_i) f_1^* \end{aligned}$$

where the last second equality is due to  $\sum_{i=1}^3 f_i = 0$ . Similarly, we have

$$\begin{aligned} \sqrt{\alpha_3} (\sum_{i=1}^3 f_i \mathbf{U}_i) l_{32}^* + \sqrt{\alpha_1} (\sum_{i=1}^3 f_i \mathbf{U}_i) l_{12}^* &= (\sum_{i=1}^3 f_i \mathbf{U}_i) f_2^* \\ \sqrt{\alpha_1} (\sum_{i=1}^3 f_i \mathbf{U}_i) l_{13}^* + \sqrt{\alpha_2} (\sum_{i=1}^3 f_i \mathbf{U}_i) l_{23}^* &= (\sum_{i=1}^3 f_i \mathbf{U}_i) f_3^*. \end{aligned}$$

Lastly,  $P^* \begin{pmatrix} \sqrt{\alpha_1} \sum_i f_i \mathbf{U}_i \\ \sqrt{\alpha_2} \sum_i f_i \mathbf{U}_i \\ \sqrt{\alpha_3} \sum_i f_i \mathbf{U}_i \end{pmatrix} = (\sum_i f_i \mathbf{U}_i) (\sum_i f_i^*) = 0$ . For the case that  $n = 1$ ,

we assume  $\mathbf{v}_1$  to be the pinned points. Structures of the four blocked matrices are:

$$\mathcal{M}_f = \begin{pmatrix} \mathcal{N}_f \\ \mathbf{0}^- \bar{f}_2^- \mathbf{0}^- \bar{f}_3^- \mathbf{0}^- \end{pmatrix}, \mathcal{M}_f^+ = \begin{pmatrix} 0 \\ \mathcal{N}_f \\ \mathbf{0} \\ \mathcal{L}^- \mathcal{P}^- \end{pmatrix}, \mathcal{M}_p = \begin{pmatrix} \mathcal{N}_p \\ \mathbf{0}^- \bar{f}_1^- \mathbf{0}^- \end{pmatrix}, \mathcal{M}_p^+ = \begin{pmatrix} \mathcal{N}_p \\ - \mathbf{0}^- - \\ \mathbf{0} \ l_{21} \ \mathbf{0} \\ \mathbf{0} \ l_{31} \ \mathbf{0} \end{pmatrix},$$



where the last three rows in  $\mathcal{M}_f^+$  and  $\mathcal{M}_p^+$  from top to bottom corresponds to  $T_1, T_2, T_3$ . In this case, three rows of  $\mathcal{L}$  have 2, 1 and 1 nonzero entries which are  $(l_{12}, l_{13}), l_{23}$  and  $l_{32}$ , respectively. And we have

$$\begin{aligned} \mathcal{M}_f^* \mathcal{M}_p \mathbf{U}_p &= \mathcal{N}_f^* \mathcal{N}_p \mathbf{U}_p + f_1 \mathbf{v}_1 \begin{pmatrix} \mathbf{0} \\ f_2^* \\ \mathbf{0} \\ f_3^* \\ \mathbf{0} \end{pmatrix}, \mathcal{M}_f^* \mathcal{M}_f \mathbf{U}_f = \mathcal{N}_f^* \mathcal{N}_f \mathbf{U}_f + (f_2 \mathbf{v}_2 + f_3 \mathbf{v}_3) \begin{pmatrix} \mathbf{0} \\ f_2^* \\ \mathbf{0} \\ f_3^* \\ \mathbf{0} \end{pmatrix} \\ \mathcal{M}_f^{+*} \mathcal{M}_p^+ \mathbf{U}_p &= \begin{pmatrix} \mathcal{N}_f^* \mathcal{N}_p \mathbf{U}_p \\ \mathbf{0} \end{pmatrix} + l_{21} \mathbf{v}_1 \begin{pmatrix} \mathbf{0} \\ l_{23}^* \\ \mathbf{0} \\ p_2^* \end{pmatrix} + l_{31} \mathbf{v}_1 \begin{pmatrix} \mathbf{0} \\ l_{32}^* \\ \mathbf{0} \\ p_3^* \end{pmatrix} \\ \mathcal{M}_f^{+*} \mathcal{M}_f^+ \begin{pmatrix} \mathbf{U}_f \\ \sum_j \alpha_j \mathbf{v}_j \end{pmatrix} &= \mathcal{M}_f^{+*} \begin{pmatrix} \mathcal{N}_f \mathbf{U}_f \\ l_{12} \mathbf{v}_2 + l_{13} \mathbf{v}_3 + p_1 \sum_j \alpha_j \mathbf{v}_j \\ l_{23} \mathbf{v}_3 + p_2 \sum_j \alpha_j \mathbf{v}_j \\ l_{32} \mathbf{v}_2 + p_3 \sum_j \alpha_j \mathbf{v}_j \end{pmatrix} = \begin{pmatrix} \mathcal{N}_f & \mathcal{L}^* \\ -\mathbf{0} & \bar{\mathcal{P}}^* \end{pmatrix} \begin{pmatrix} \mathcal{N}_f \mathbf{U}_f \\ \sqrt{\alpha_1} \sum_j f_j \mathbf{v}_j \\ l_{23} \mathbf{v}_3 + p_2 \sum_j \alpha_j \mathbf{v}_j \\ l_{32} \mathbf{v}_2 + p_3 \sum_j \alpha_j \mathbf{v}_j \end{pmatrix} \end{aligned}$$

Again we have  $\mathcal{M}_f^* \mathcal{M}_p \mathbf{U}_p = -\mathcal{M}_f^{+*} \mathcal{M}_p^+ \mathbf{U}_p$ , to show  $\mathcal{M}_f^{+*} \mathcal{M}_f^+ \mathbf{U}_f = -\mathcal{M}_f^{+*} \mathcal{M}_p^+ \mathbf{U}_p$  and to validate this case, it is equivalent to show

$$\begin{pmatrix} \mathcal{L}^* \\ -\bar{\mathcal{P}}^* \end{pmatrix} \begin{pmatrix} \sqrt{\alpha_1} \sum_j f_j \mathbf{v}_j \\ l_{23} \mathbf{v}_3 + p_2 \sum_j \alpha_j \mathbf{v}_j \\ l_{32} \mathbf{v}_2 + p_3 \sum_j \alpha_j \mathbf{v}_j \end{pmatrix} + l_{21} \mathbf{v}_1 \begin{pmatrix} \mathbf{0} \\ l_{23}^* \\ \mathbf{0} \\ p_2^* \end{pmatrix} + l_{31} \mathbf{v}_1 \begin{pmatrix} \mathbf{0} \\ l_{32}^* \\ \mathbf{0} \\ p_3^* \end{pmatrix} = \left( \sum_{j=1}^3 f_j \mathbf{v}_j \right) \begin{pmatrix} \mathbf{0} \\ f_2^* \\ \mathbf{0} \\ f_3^* \\ \mathbf{0} \end{pmatrix}$$

and we have .

$$\begin{aligned} &(\sqrt{\alpha_1} \sum_j f_j \mathbf{v}_j) l_{12}^* + (l_{32} \mathbf{v}_2 + p_3 \sum_j \alpha_j \mathbf{v}_j + l_{31} \mathbf{v}_1) l_{32}^* \\ &= \left( \sum_j f_j \mathbf{v}_j \right) (\alpha_1 f_2^* - \alpha_2 f_1^*) + \frac{1}{\alpha_3} (\alpha_3 f_2^* - \alpha_2 f_3^*) \cdot \left[ (\alpha_3 f_2 - \alpha_2 f_3) \mathbf{v}_2 + f_3 \sum_j \alpha_j \mathbf{v}_j + (\alpha_3 f_1 - \alpha_1 f_3) \mathbf{v}_1 \right] \\ &= \left( \sum_j f_j \mathbf{v}_j \right) [(\alpha_1 f_2^* - \alpha_2 f_1^*) + (\alpha_3 f_2^* - \alpha_2 f_3^*)] = \left( \sum_j f_j \mathbf{v}_j \right) (\alpha_1 f_2^* + \alpha_2 f_2^* + \alpha_3 f_2^*) = \left( \sum_j f_j \mathbf{v}_j \right) f_2^* \end{aligned}$$

where the last two equalities are due to  $\sum_j f_j = 0$ . Similarly, we have

$$(\sqrt{\alpha_1} \sum_j f_j \mathbf{v}_j) l_{13}^* + (l_{23} \mathbf{v}_3 + p_2 \sum_j \alpha_j \mathbf{v}_j + l_{21} \mathbf{v}_1) l_{23}^* = \left( \sum_j f_j \mathbf{v}_j \right) f_3^*,$$

And for the last row,

$$\begin{aligned} &p_1^* (\sqrt{\alpha_1} \sum_j f_j \mathbf{v}_j) + p_2^* (l_{23} \mathbf{v}_3 + p_2 \sum_j \alpha_j \mathbf{v}_j) + p_3^* (l_{32} \mathbf{v}_2 + p_3 \sum_j \alpha_j \mathbf{v}_j) + l_{21} \mathbf{v}_1 p_2^* + l_{31} \mathbf{v}_1 p_3^* \\ &= f_1^* \left( \sum_j f_j \mathbf{v}_j \right) + p_2^* (l_{23} \mathbf{v}_3 + p_2 \sum_j \alpha_j \mathbf{v}_j + l_{21} \mathbf{v}_1) + p_3^* (l_{32} \mathbf{v}_2 + p_3 \sum_j \alpha_j \mathbf{v}_j + l_{31} \mathbf{v}_1) \\ &= f_1^* \left( \sum_j f_j \mathbf{v}_j \right) + f_2^* \left( \sum_j f_j \mathbf{v}_j \right) + f_3^* \left( \sum_j f_j \mathbf{v}_j \right) = (f_1 + f_2 + f_3)^* \left( \sum_j f_j \mathbf{v}_j \right) = 0 \end{aligned}$$

Using the same argument, we can easily validate the case  $n = 2$ .

This provides a theoretic support for us to compute the deformation of a finer mesh via interpolation on the coarser mesh.

Given face-wise constant BC  $\mu = \{\mu_T : T \in F\}$ , we define an operator  $\mathcal{F}$  as the LSQC solution, i.e.  $f = \mathcal{F}(\mu, p_1, p_2, q_1, q_2)$  such that  $f(p_i) = q_i$ . And the optimization problem in 1 is equivalent to:

$$\min_{(\mu, p_i, q_i)} \mathcal{L}(\mu, p_i, q_i) = \min_{(\mu, p_i, q_i)} E_1(\mathcal{F}(\mu, p_1, p_2, q_1, q_2)) + E_2(\mu) \quad \text{s.t. } \|\mu\|_\infty < 1, p_i \in \mathbb{D}, q_i \in \mathbb{C},$$

where  $E_1$  drives task-specific objectives and  $E_2$  is a regularizer of BC  $\mu$ . This dual-energy approach enables fine-tuned control over the quasiconformal mapping's geometric properties without compromising its task-oriented performance.

With these advantages, LSQC should have been a perfect tool to derive a free-boundary non-overlapping map. However, there is a drawback in this method. Since  $\mathcal{F}$  involves solving a huge sparse linear system, it is computationally expensive or impossible to backpropagate the gradient of loss function  $\mathcal{L}$  w.r.t the mapping  $\frac{\partial \mathcal{L}}{\partial f}$  to that w.r.t BC  $\frac{\partial \mathcal{L}}{\partial \mu}$ , the pinned points  $\frac{\partial \mathcal{L}}{\partial p_i}$  and their destinations  $\frac{\partial \mathcal{L}}{\partial q_i}$ , strictly following the chain rule. The Alternating Direction Method of Multipliers (ADMM) partially mitigates this by updating  $\mu$  based on the BCs reconstructed from the newly updated mapping  $f$ , but it does not address the lack of explicit gradients for pinned points  $p_i$  and destinations  $q_i$ . Previous approaches, such as those by Qiu [34, 35] circumvent this by imposing destinations of certain points in advance, which is often unrealistic in real-life scenarios.

## 6 Spectral Beltrami Network

To overcome these limitations, we propose the Spectral Beltrami Network (SBN), a differentiable neural surrogate for  $\mathcal{F}$  that enables gradient backpropagation through  $\mu$  and  $p$ . The network operates on the unit disk  $\mathbb{D}$ , naturally following formulation 1. We represent the domain as a triangular mesh viewed as a directed graph  $\mathcal{G} = (V, E, F)$  with nodes  $V$ , directed edges  $E$ , and faces  $F$ . SBN leverages three nested meshes  $\mathcal{G}^i = (V^i, E^i, F^i)$  ( $i = 1, 2, 3$ ) of decreasing resolution. Given BC  $\mu_v$  on all  $v \in V^1$  and two points  $p_1, p_2 \in V^1$ , the network predicts a mapping  $F$  approximating the numerical LSQC solution  $f$  of  $\{\mu_T : T \in F^1, \mu_T = \frac{1}{3} \sum_{v \in T} \mu_v\}$  with fixed constraints  $f(p_i) = p_i, i = 1, 2$ . Enforcing selected two points to be fixed is based on two practical considerations. First, it constrains the output range, preventing training instabilities from unbounded target positions. Second, arbitrary target positions  $q_1, q_2$  can be recovered via post-composition with a similarity transformation  $g$  satisfying  $g(p_j) = q_j$  ( $j = 1, 2$ ). By Prop.2,  $\mathcal{F}(\mu, p_1, p_2, q_1, q_2) = g \circ \mathcal{F}(\mu, p_1, p_2, p_1, p_2)$ , ensuring no loss of generality.

Therefore, in downstream applications after the SBN is well trained, parameters to be optimized include BC, coordinates of two fixed points, and parameters for scaling, rotation and translation. The challenge lies in incorporating the BC and pinned point information into the network and building

efficient short- and long-range interactions between vertices, depicting the dynamics of LSQC energy.

### 6.1 Encoding input information

SBN operates on three types of graphs: meshes ( $\mathcal{G}^i, i = 1, 2, 3$ ), downsampling graphs ( $\mathcal{G}^{\text{down},i} = (V_i \cup V_{i+1}, E^{i,i+1})$ ), and upsampling graphs ( $\mathcal{G}^{\text{up},i} = (V_i \cup V_{i+1}, E^{i+1,i})$ ) for  $i = 1, 2$ . Each vertex  $v \in V_1$  is assigned BC  $\mu_v$  and encoded with a 13-dim feature vector  $\tilde{v} = [\mu_v, K_v, \arg(\mu_v), |\mu_v|, v - p_1, \|v - p_1\|_2, v - p_2, \|v - p_2\|_2, v]$  where  $K_v = \frac{1+|\mu_v|}{1-|\mu_v|}$  captures distortion and the pinned-point features encode positional relationships. An encoder MLP maps  $\tilde{v}$  to 24-dim embeddings. For coarser meshes ( $V_2, V_3$ ), if  $v = \sum_{j=1}^3 \lambda_j v_j$  with  $v_j \in V_1$  and  $\sum_j \lambda_j = 1$ , then  $\mu_v = \sum_{j=1}^3 \lambda_j \mu_{v_j}$  by barycentric interpolation, yielding analogous 24-dim embeddings. Edge features are computed as  $e_{i,j}^{k,l} = f_e^{\text{en}}(\tilde{v}_j - \tilde{v}_i, \|v_j - v_i\|_2)$  for edges from  $v_i \in V^k$  to  $v_j \in V^l$ , where  $f_e^{\text{en}}$  is an encoding MLP capturing directed vertex differences. Superscripts  $(k, l)$  are omitted when clear from context.

### 6.2 Message Passing Mechanism

We adapted the multiscale message passing from [12] and improved the way of hierarchical edge construction. For downsampling graph  $\mathcal{G}^{\text{down},i} = (V^i \cup V^{i+1}, E^{i,i+1})$ , each node  $v_k \in V^i$  is connected to the three corners of its containing triangle in  $V^{i+1}$  (identified by minimal  $|\alpha_{k,l}| + |\alpha_{k,m}| + |\alpha_{k,n}|$  in barycentric coordinates  $v_k = \alpha_{k,l}v_l + \alpha_{k,m}v_m + \alpha_{k,n}v_n$ ). Considering the free-boundary nature of LSQC, it is crucial to enhance boundary information exchange and thus we add edges from fine-mesh boundary nodes to any coarse-mesh vertex within a distance threshold. Upsampling graph  $\mathcal{G}^{\text{up},i} = (V^i \cup V^{i+1}, E^{i+1,i})$  reverses edge directions. See Fig.1. The general update Rules for node and edge embeddings are as follows: For graph  $\mathcal{G}$  with edges  $(v_i, v_j)$  where  $v_i \in V^k, v_j \in V^l$ :

$$e_{i,j} = f_e^{k,l}(e_{i,j}, v_i, v_j, \theta_e), \quad v_j = f_v^{k,l}\left(v_j, \sum_{e_{i,j} \in E^{k,l}} e_{i,j}, \theta_v\right).$$

Update Rules are applied sequentially to  $\mathcal{G}^k$  (intra-mesh,  $k = l$ ),  $\mathcal{G}^{\text{down},k}$  (fine-to-coarse,  $k < l$ ), and  $\mathcal{G}^{\text{up},k}$  (coarse-to-fine,  $k > l$ ). Here  $f_e, f_v$  are residual MLPs [18] with GraphNorm [6]; parameters  $\theta_e, \theta_v$  encode PDE constraints for robustness. This multiscale mechanism extends interaction ranges, allowing each node to reach the entire mesh through hierarchical edges and enhanced boundary broadcasting Fig.2 is the architecture of a message passing block.

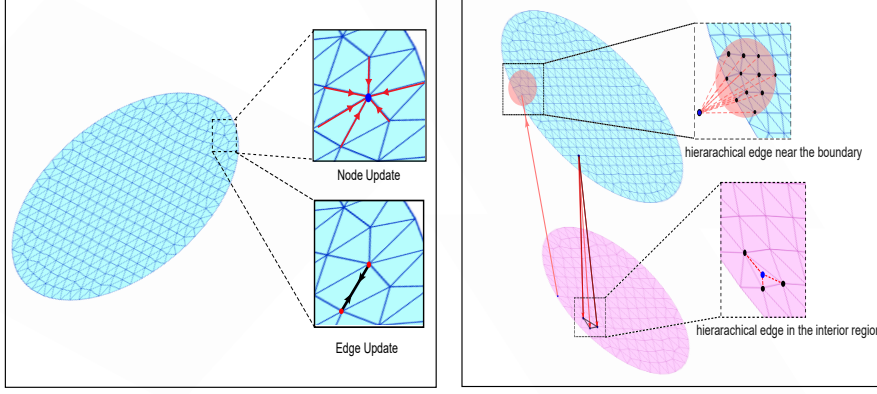


Fig. 1: Illustration of the embedding update rule and the hierarchical edge construction.

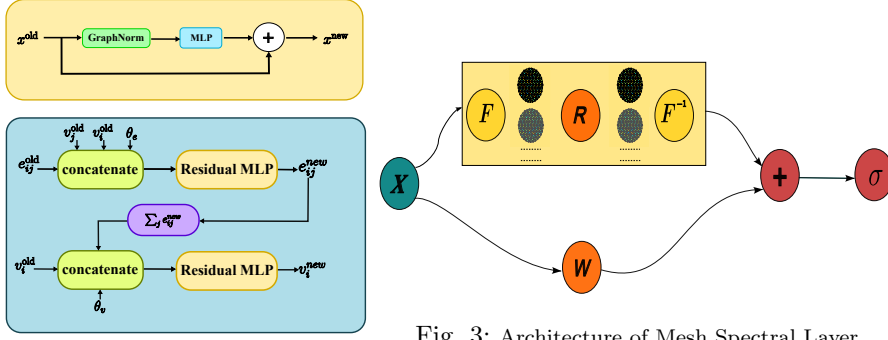


Fig. 2: Architecture of Message Passing Block.

Fig. 3: Architecture of Mesh Spectral Layer

### 6.3 Mesh Spectral Layer

A critical limitation persists: purely local message passing struggles to propagate information between distant nodes, especially in dense meshes where signals attenuate over multiple iterations. This is particularly problematic for our free-boundary problem, where pinned-point positions exert global influence on the mapping. Experimentally, we observed that multiscale message passing alone risks neural collapse, producing near-identity outputs. Inspired by Fourier Neural Operator (FNO) [25], we proposed the Mesh Spectral Layer (MSL) to capture global dependencies via the mesh Laplacian’s eigenbasis. For a triangular mesh  $(V, E, F)$  with Laplacian  $\Delta = \mathbf{M}^{-1}\mathbf{L}$ , where

$$\mathbf{L}_{ij} = \begin{cases} \frac{1}{2}(\cot \alpha_{ij} + \cot \beta_{ij}) & \text{if } j \sim i \\ -\sum_{j' \in \mathcal{N}(i)} w_{ij'} & \text{if } j = i \\ 0 & \text{otherwise} \end{cases}, \quad \mathbf{M}_{ik} = \begin{cases} \frac{1}{3} \sum_{T_j \in \mathcal{N}(i)} \text{area}(T_j) & \text{if } i = k \\ 0 & \text{otherwise} \end{cases},$$

where  $\alpha_{ij}$  and  $\beta_{ij}$  are the angles opposite to the edge  $[i, j]$  and  $\mathcal{N}(i)$  is the list of adjacent vertices and faces of the vertex  $i$ . Since  $\Delta$  is symmetric positive semi-definite and encodes mesh geometry, we project latent features  $X \in \mathbb{R}^{|V| \times d}$  onto

its  $k$  smallest eigenvectors  $F \in \mathbb{R}^{k \times |V|}$ , performing spectral-domain mixing:

$$X \leftarrow \sigma(XW + F^T(R \cdot (FX))), \quad (R \cdot (FX))_{jl} = \sum_{n=1}^d R_{jln}(FX)_{jn}$$

with trainable  $W \in \mathbb{R}^{d \times \tilde{d}}$  and  $R \in \mathbb{R}^{k \times \tilde{d} \times d}$ . This offers efficient global communication with far fewer parameters than attention mechanisms [39]. Fig.3 shows the architecture of this module.

#### 6.4 Model architecture and training

A key principle in combining global operators with local message passing is that each node should carry structural information beyond individual messages. Fig.4 shows the complete SBN architecture integrating multiscale message passing and MSLs.

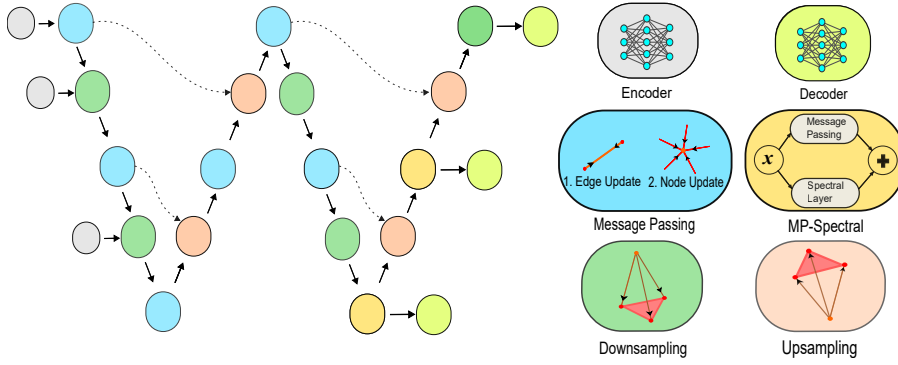


Fig. 4: Architecture of Spectral Beltrami Network

SBN is trained by supervising the predicted mapping  $\hat{u} = \mathcal{F}_\theta(\mu_{V^1}, p_1, p_2)$  against ground-truth  $u = \mathcal{F}_\theta(\mu_{F^1}, p_1, p_2, p_1, p_2)$  where  $\mu_{F^1} = \{\mu_T | \mu_T = \frac{1}{3} \sum_{v \in T} \mu_v, T \in F^1\}$ , via four loss components:

1. **Boundary-weighted node loss** emphasizes boundary accuracy where free-boundary errors concentrate:

$$\mathcal{L}_1(V^1) = \frac{1}{|V^1|} \sum_{v \in V^1} e^{\|u(v)\|_2} \|u(v) - \hat{u}(v)\|_2^2.$$

2. **Relative edge deformation loss** prevents mesh folding by penalizing inconsistent edge deformations:

$$\mathcal{L}_2(E^1) = \frac{1}{|E^1|} \sum_{[i,j] \in E^1} \frac{\|(\hat{u}(v_i) - \hat{u}(v_j)) - (u(v_i) - u(v_j))\|_2}{\|u(v_i) - u(v_j)\|_2}.$$

3. **Boundary  $L_1$  loss** provides robust boundary fitting:

$$\mathcal{L}_3(\partial V^1) = \frac{1}{|\partial V^1|} \sum_{v \in \partial V^1} \|u(v) - \hat{u}(v)\|_1.$$

4. **Deep supervision** extends losses to coarser meshes  $V^2, V^3$  (with interpolated ground-truth) to enhance gradient flow and representation learning:

$$\mathcal{L}_1^{ds}(V^1, V^2, V^3) = \mathcal{L}_1(V^1) + \lambda_2(t)\mathcal{L}_1(V^2) + \lambda_3(t)\mathcal{L}_1(V^3),$$

where  $\lambda_j(t) = \lambda \cdot \frac{t}{N} + \lambda_j \cdot (1 - \frac{t}{N})$  gradually decays coarse-mesh influence ( $\lambda_2 = \lambda_3 = 0.2, \lambda = 0.1$ ).

In conclusion, the total training loss is a weighted sum of these loss terms. Once the training of SBN was finished, we obtained a neural network  $\mathcal{F}_{\theta^*}$  and in the optimization problem, its parameters are frozen.

## 7 SBN-Opt: A novel optimization framework of the free-boundary diffeomorphism problem

A well trained SBN  $\mathcal{F}_{\theta^*}$  serves as a differentiable solver for optimization of free-boundary diffeomorphism. We optimize input BC  $\{\mu_v\}$ , pinned points  $\{p_1, p_2\}$ , and post-composition similarity parameters  $(\phi, s, r)$  to minimize task-specific energies. To ensure valid inputs ( $\|\mu_v\|, \|p_i\| < 1$ ), we apply an activation function:

$$\mathcal{T}(x, T) = \left( \frac{e^{\frac{|x|}{T}} - e^{-\frac{|x|}{T}}}{e^{\frac{|x|}{T}} + e^{-\frac{|x|}{T}}} \right) e^{i \arg(x)},$$

setting  $\mu_v = \mathcal{T}(\tilde{\mu}_v, T_{\text{BC}})$  and  $p_i = \mathcal{T}(\tilde{p}_i, T_{\text{pin}})$  where  $(\tilde{\mu}_v, T_{\text{BC}}, \tilde{p}_i, T_{\text{pin}})$  are unconstrained optimization variables. In this way, we introduce the SBN guided optimization framework SBN-Opt for solving the problem 1

$$\min_{(\tilde{\mu}_v, T_{\text{BC}}, \tilde{p}_i, T_{\text{pin}}, \phi, s, r)} E_1(g(\mathcal{F}_{\theta^*}(\mu_v, p_1, p_2), \phi, s, r)) + E_2(\mu), \quad g(x, \phi, s, r) = se^{i\phi}x + r.$$

Direct optimization on BC enables explicit distortion control via  $E_2(\mu)$ . For instance, angle distortion is penalized by  $E_{\text{BC}} = \frac{1}{|V^1|} \sum_{v \in V^1} |\mu_v|^2$ , while smoothness (assuming piecewise-linear  $\mu$ ) is enforced via  $E_{\text{smooth}} = \frac{1}{|F^1|} \sum_{T \in F^1} |\nabla \mu(T)|^2$ . Although SBN outputs only on  $V^1$ , any point  $v \in \mathbb{D}$  maps via barycentric interpolation. By resolution-independence (Prop. 3), this remains faithful to the continuous solution. For each vertex in a high-resolution mesh  $v_p \in V^{\text{orig}}$ , we identify the triangle  $I(p) = [v_i, v_j, v_k] \in F^1$  that minimizes  $|\lambda_i| + |\lambda_j| + |\lambda_k|$  among barycentric representations  $v_p = \lambda_i v_i + \lambda_j v_j + \lambda_k v_k$  (with  $\lambda_i + \lambda_j + \lambda_k = 1$ ) in all triangles, and this identifies the containing triangle where all coordinates are non-negative. We precompute a sparse interpolation matrix  $R \in \mathbb{R}^{|V^{\text{orig}}| \times |V^1|}$  where

$$R_{p,q} = \begin{cases} \lambda_q(v_p) & \text{if } v_q \text{ is a vertex of the identified triangle,} \\ 0 & \text{otherwise,} \end{cases}$$

enabling per-iteration interpolation  $f(V^{\text{orig}}) = R \cdot f(V^1)$  and the computation cost and memory is negligible relative to the forward pass of SBN.

Next, we take the tasks in Sec.9 as examples to illustrate how to apply the framework 7. In the **density equalizing mapping problem**, given a triangular mesh  $\mathcal{T} = (V, F)$  of  $\mathbb{D}$  with population  $\{p(T) : T \in F\}$ , we seek a homeomorphism  $f : \mathbb{D} \rightarrow \mathbb{R}^2$  making density  $\rho(f(T)) = \frac{p(T)}{\text{Area}(f(T))}$  uniform across faces. If without setting up a sea surrounding the disk, the region might arbitrary expand. However, setting up a sea might restrict the movement of the true boundary and make the area change near the true boundary damped. Instead, if needed, we can easily discourage arbitrary expansion of the region by designing a barrier function on the scaling parameter  $s$  in the framework 7.

$$E_1 = \sum_{T \in F} (\rho(T) - \bar{\rho}(f))^2 + \lambda_{\text{reg}} R_{\text{barrier}}(s), \quad R_{\text{barrier}}(s) = \max\{0, s - \omega\},$$

where  $\bar{\rho}(f) = \frac{\sum_T p(T)}{\sum_T \text{Area}(f(T))}$  is the target density. The total area is efficiently computed via Green's theorem:  $\sum_T \text{Area}(f(T)) = \frac{1}{2} \sum_{[v_i, v_j] \in \partial \mathbb{D}} (f(v_i)_1 f(v_j)_2 - f(v_i)_2 f(v_j)_1)$ .

In the work [35], Qiu et al. developed an efficient splitting method based on Alternating Direction Method with Multipliers (ADMM) to apply the numerical LSQC algorithm in the **inconsistent surface registration problem**. However, the algorithm relies on prescribed landmark point-to-point correspondence. One of advantages in our framework is that the pinned points itself are also optimization parameters therefore it can be applied to more general inconsistent surface registration problems. In practice, exact point to point correspondence is usually impractical and unreasonable. For one thing, manually labeling point to point correspondence is time-consuming. For another, measurement noise, meshing artifacts and smoothing alter vertex positions by millimeters thus treating those vertices as hard truths injects error. Therefore, it is more common to relax the correspondence to the relation between point sets and point sets. Given surfaces  $S_1, S_2$  with subsets  $\{S_{i,j}\}$  and intensity functions  $I_i : S_i \rightarrow \mathbb{R}$ , we seek a diffeomorphism  $f : S_1 \rightarrow \mathbb{R}^3$  and optimal regions  $\Omega_i^* \subset S_i$  minimizing:

1. Intensity mismatch:  $E_I(f, \Omega_1) = \int_{f(\Omega_1)} \|(I_1 \circ f^{-1} - I_2)\|_1 dA$
2. Point-set discrepancy (via chamfer distance):

$$E_{\text{pc}}(f) = \sum_j \left( \frac{1}{|S_{1,j}|} \sum_{v \in S_{1,j}} \min_{w \in S_{2,j}} \|f(v) - w\|^2 + \frac{1}{|S_{2,j}|} \sum_{w \in S_{2,j}} \min_{v \in S_{1,j}} \|w - f(v)\|^2 \right).$$

After conformally parameterizing  $S_i$  to  $\mathbb{D}$ , the problem reduces to finding the optimal  $f : \mathbb{D} \rightarrow \mathbb{R}^2$  under the maximality assumption  $f(\Omega_1) = \Omega_2 = f(S_1) \cap S_2$ . We minimize  $E_1 = \lambda_I E_I + \lambda_{\text{pc}} E_{\text{pc}}$  while  $E_2(\mu)$  provides distortion regularization. For the general optimization problem, we have the following algorithm.

*Remark 1* In practice, a disk conformal parameterization is not mandatory. To avoid unnecessary conformal distortion caused by the fixed boundary shape,

**Algorithm 1** SBN-Opt

---

**Input:** Data: A triangular mesh  $\mathcal{T} = (V, F)$  of the unit disk  $\mathbb{D}$ . Parameters to be optimized:

1. Optimization parameters  $\eta$  include  $\tilde{\mu}_v$ ,  $T_{\text{BC}}$ ,  $\tilde{p}_i (i = 1, 2)$ ,  $T_{\text{pin}}$ , log of scaling  $\tilde{s}$ , rotation angle  $\phi$  and translation vector  $r$ .
2. Loss weights  $\lambda_j$ , energy functionals  $E_j$  and optimizer  $\Psi$ .

**Output:** Deformed mesh  $f(\mathcal{T}) = (f(V), F)$

- 1: Freeze the parameters of SBN  $\mathcal{F}_{\theta^*}$ .
- 2: Compute and save the interpolation matrix  $R \in \mathbb{R}^{|V| \times |V_1|}$
- 3: *continue* = *True*;
- 4: **while** *continue* **do**
- 5:   Prepare input  $\mu = \mathcal{T}(\tilde{\mu}, T_{\text{BC}})$ ,  $p_i = \mathcal{T}(\tilde{p}_i, T_{\text{pin}})$  for the model  $\mathcal{F}_{\theta^*}$ .
- 6:   Obtain the mappings  $f(V^1) = g(\mathcal{F}_{\theta^*}(\mu_v, p_1, p_2), \phi, e^{\tilde{s}}, r) \in \mathbb{C}^{|V^1| \times 1}$  and the deformed mesh  $f(V) = R f(V^1)$ .
- 7:   Compute the weighted sum  $E$  of losses  $E_1(f(V))$  and  $E_2(\mu)$  with weights  $\lambda_1, \lambda_2$ .
- 8:   **if**  $E$  and  $E_j$  meet stop criterion **then**
- 9:     *continue* = *False*;
- 10:   **else**
- 11:     Compute  $\frac{\partial E}{\partial \eta}$  for all parameters  $\eta$  and then update all  $\eta$  with the optimizer  $\Psi$ .
- 12:   **end if**
- 13: **end while**

---

sometimes we use the method in [24] to compute the free-boundary conformal parameterization of a surface. Again, due to Prop.3 and Prop.2, we can still compute the deformation by interpolation. The idea is that, let  $\psi : S \rightarrow \mathbb{R}^2$  be a conformal parameterization of the surface  $S$ ,  $r_0 = \max_{v \in S} \|\psi(v)\|_2$  and  $R$  is the sparse interpolation matrix of  $f(S)$  with respect to the mesh  $r_0 \cdot \mathbb{D} = (r_0 \cdot V^1, F^1)$ , if  $f : V^1 \rightarrow \mathbb{R}^2$  is a deformation predicted by SBN, then deformation of  $\psi(S)$  is  $r_0 \cdot R f(V^1)$ .

## 8 Implementation

We implemented all experiments, including the training of SBN and downstream applications, using the PyTorch framework [31]. The SBN model was trained in a supervised manner, with numerical solutions from the Least Squares Quasiconformal Energy (LSQC) solver serving as ground-truth mappings. The training dataset comprised 960 images from the ILSVRC2012 dataset [37], which provided realistic BCs with both low- and high-frequency components. To generate BCs, we randomly selected two images per training iteration, applied data augmentation techniques (random flipping, noise addition, and blurring), and normalized them to form the real and imaginary parts of the BCs. Two pinned points were randomly chosen from the vertices of the finest mesh for each training sample.

SBN employs a hierarchical architecture. It integrates two core components: multiscale message-passing mechanism and mesh spectral layer, as detailed in Sec.6. The numbers of message passing numbers per scale depends on the mesh resolution, which are 3,3,5 from high to low, and the number of MSL per scale is 2. The training process ran for 250 epochs using the AdamW



optimizer [26] with parameters  $\beta = (0.9, 0.999)$ , a weight decay of  $1 \times 10^{-2}$ , an initial learning rate  $3 \times 10^{-4}$ . We used three triangular meshes of varying resolutions, generated with the MATLAB DistMesh function [32], with initial edge lengths of 0.015, 0.3, and 0.5. The numbers of vertices and faces in these three meshes with resolution from high to low are (16114, 31803), (4027, 7846) and (1452, 2774), respectively. The loss function for training SBN combined three terms  $\mathcal{L}_i^{ds}$  ( $i = 1, 2, 3$ ) with weights all 1. Although we did not perform an exhaustive grid search for optimal hyperparameters, this configuration yielded strong performance, as demonstrated in Sec.9. All experiments were conducted on an NVIDIA A40 GPU with 44GB memory, ensuring efficient computation.

## 9 Experimental results

Numerical experiments were conducted to evaluate the efficacy and potential of SBN. Given that SBN’s performance depends on its ability to accurately predict mappings for various BCs  $\mu$ , we first compare its predicted outputs with numerical solutions. This is followed by several applications in density equalizing and inconsistent surface registration, encompassing both realistic and synthetic scenarios.

### 9.1 Performance of Spectral Beltrami Network

SBN, trained over 250 epochs, achieves robust simulation of the Beltrami equation. Under typical conditions (BC with norms mostly below 0.4), it achieves the average nodewise L2 error smaller than 0.03, relative to numerical LSQC solutions, demonstrating strong generalizability on unseen data (Fig.5). The model maintains robustness in challenging scenarios involving larger BC norms (Fig.6) or significant domain domain distortions (Fig.7), effectively handling complex or large deformations.

A self-ablation study was conducted to investigate individual contributions of the multiscale message-passing mechanism and the mesh spectral layer (MSL) within our architecture. Removing MSL yields Multiscale MeshGraphNet (M-MGN) [12]; using only MSL gives Mesh Spectral Net (MSN). Across all three test cases (Figs.5-7), SBN significantly outperforms both ablations, confirming the synergy between multiscale message passing and spectral layers.

To further evaluate SBN, we compared it with M-MGN, MSN, and the numerical LSQC algorithm, running tests across 10,000 sets of BCs and pinned points. Two regimes were studied: (1) maximum BC L2 norm less than 0.4, and (2) maximum BC L2 norm between 0.4 and 0.8. We measure: non-injective triangles (faces with negative Jacobian), nodewise L2 error, boundary L2 error, and BC L2 error (vs. target face-averaged BCs). Tables 1–2 show that SBN achieves the lowest errors and fewest fold-overs, closely matching numerical LSQC accuracy while substantially outperforming M-MGN and MSN in both regimes.

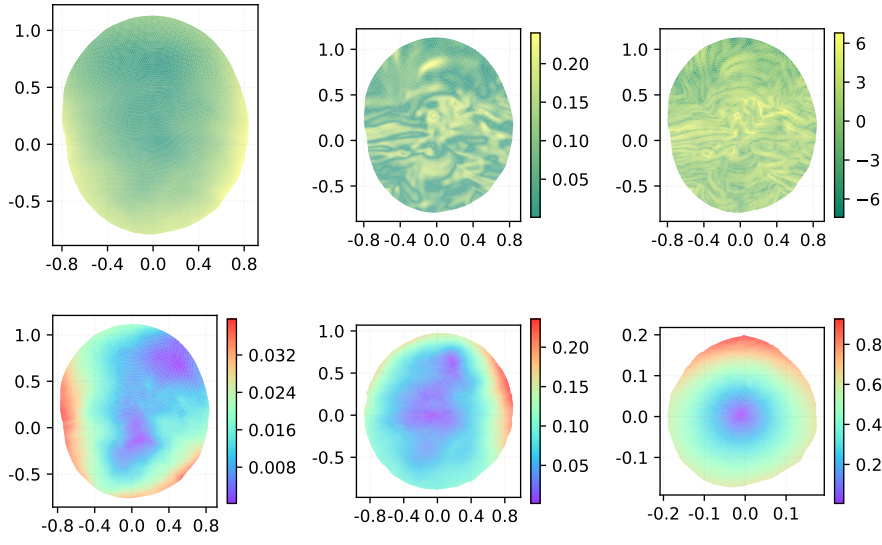


Fig. 5: Comparison of SBN, M-MGN, and MSN for typical cases (max BC norm  $\leq 0.4$ ). Top row: numerical solution field (left), BC magnitude (center), log gradient magnitude of BCs (right). Bottom row: color-coded nodewise L2 errors for SBN, M-MGN, and MSN vs. reference solution. Format applies to Figs.6 and 7.

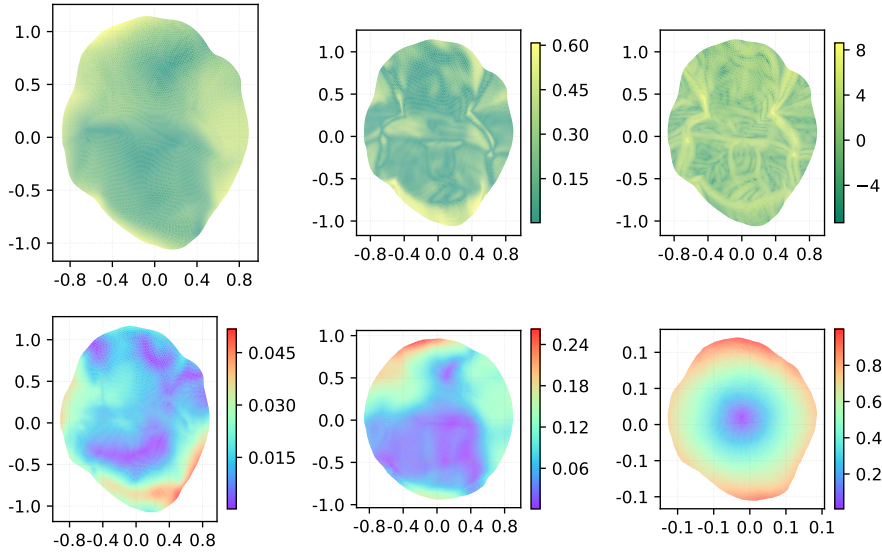


Fig. 6: Comparison of three models (SBN, M-MGN and MSN) for simulating LSQC in the case that BCs' range is larger.

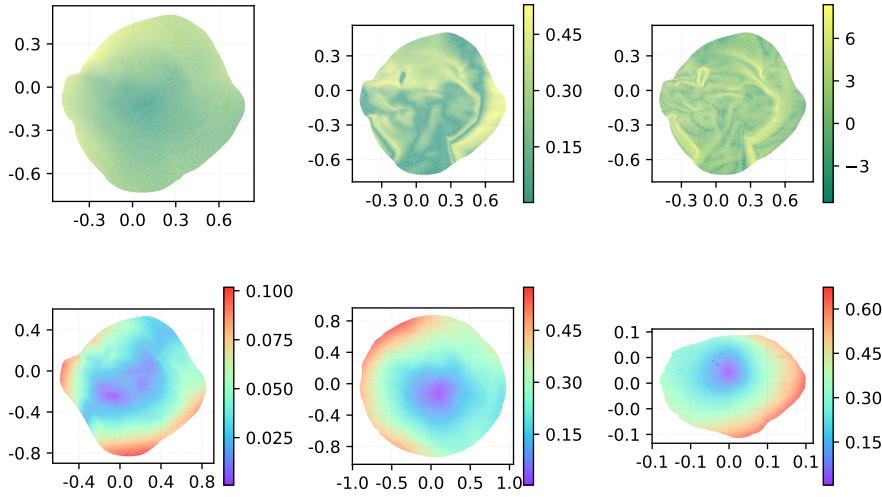


Fig. 7: Comparison of three models (SBN, M-MGN and MSN) for simulating LSQC in the case that the desired mapping is a large distortion.

Table 1: Performance for Case 1 (maximum BC norm is smaller than 0.4), averaged over 10,000 tests. Lower values indicate better performance.

Method	Non-injective Triangles	Nodewise L2 Error	Boundary L2 Error	BC L2 Error
LSQC	0.00050	—	—	0.00348
SBN	0.09560	<b>0.02239</b>	<b>0.03352</b>	0.02306
M-MGN	0.38050	0.09481	0.15194	0.07031
MSN	33.2049	0.49009	0.73313	0.09514

Table 2: Performance for Case 2 (max BC norm is between 0.4 and 0.8), averaged over 10,000 tests. Lower values indicate better performance.

Method	Non-injective Triangles	Nodewise L2 Error	Boundary L2 Error	BC L2 Error
LSQC	0.24530	—	—	0.01146
SBN	1.28710	<b>0.04671</b>	<b>0.07217</b>	0.07679
M-MGN	23.5595	0.23172	0.37515	0.19477
MSN	264.365	0.47382	0.70073	0.18091

## 9.2 Density Equalizing parameterization

We demonstrate SBN-Opt’s superiority over numerical methods [9] in both density equalization and conformal distortion control. Problem formulation details are in Sec.7.

### 9.2.1 Simply Connected Cases

We begin with two simply connected examples. First is a synthetic example of a peak. In this example, the weights of task loss  $E_1$ , angle distortion loss  $E_{BC}$  and

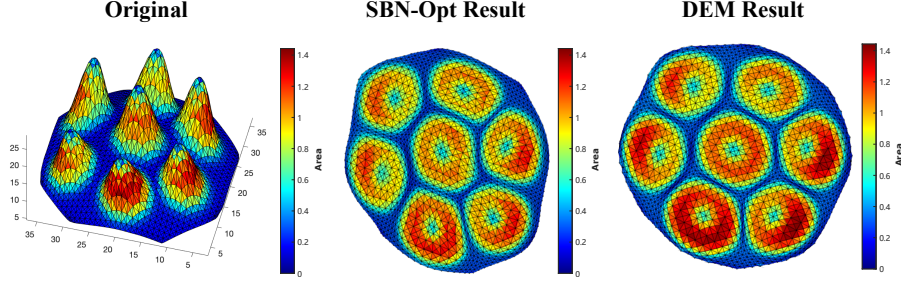


Fig. 8: Density equalizing parameterization of the "peak" model. From left to right: The original 3D mesh, the parameterization result from our SBN-Opt, and the result from the DEM algorithm. All meshes are colored according to face area, where warmer colors indicate larger areas.

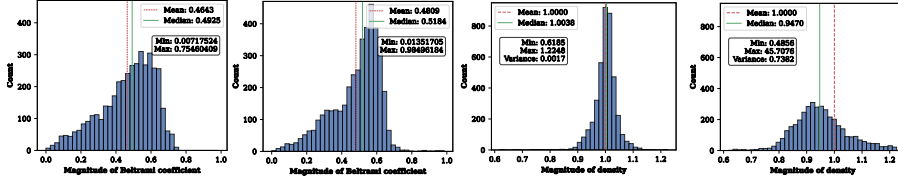


Fig. 9: Statistical comparison of parameterization results for the "peak" model. From left to right: (a) Histogram of BC magnitudes from our method; (b) Histogram of BC magnitudes from DEM; (c) Histogram of the face density distribution from our method; and (d) Histogram of the face density distribution from DEM. Note that the histogram for the DEM density distribution (d) is truncated to the density range of our method's result to enable a direct comparison, as the DEM result contains significant outliers.

smoothness loss  $E_{\text{smooth}}$  are 1,  $5e-2$  and  $1e-3$ , respectively. The result mappings of our method and DEM [9] are shown in Fig.8. In Fig.9, we compared our result with DEM's result in two aspects, distribution of angle distortion and performance in density equalizing  $\rho(T) = \frac{\text{Area}(f(T))}{\text{Area}(T)}$ . Our SBN-Opt achieved a more uniform density distribution, reducing the variance of face density from 0.7382 to a mere 0.0017. Simultaneously, it produced a mapping with lower angular distortion, as evidenced by a 3.5% reduction in the average L2 norm of the resulting BCs (from 0.481 to 0.464).

The second example is a lion face. In this example, the weights of task loss  $E_1$ , angle distortion loss  $E_{\text{BC}}$  and smoothness loss  $E_{\text{smooth}}$  are 1,  $1e-2$  and  $1e-3$ , respectively. The result mappings of our method and DEM are shown in Fig.10. As shown in Fig.9, the improvements were even more pronounced. Our method decreased the average L2 norm of the BCs by 11.6% (from 0.405 to 0.358), indicating substantially less conformal distortion than the DEM result. The final density distribution was also highly concentrated around the target, with its variance decreasing significantly to 0.0062. Across all cases, SBN-Opt consistently outperforms DEM in both density equalization and angular distortion reduction. DEM's higher variance stems from outlier faces

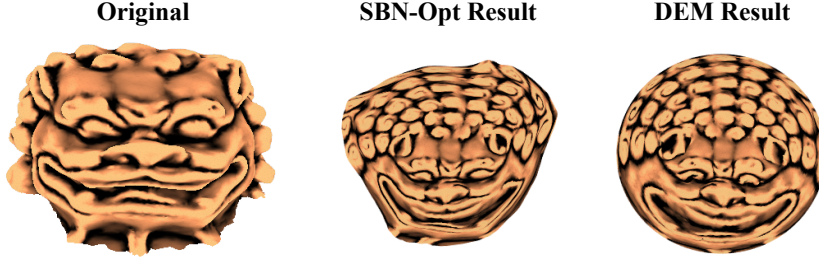


Fig. 10: Density equalizing parameterization of the "lion face" model. From left to right: The original 3D mesh, the parameterization result from our SBN-Opt, and the result from the DEM algorithm. All meshes are colored according to mean curvature for visualization.

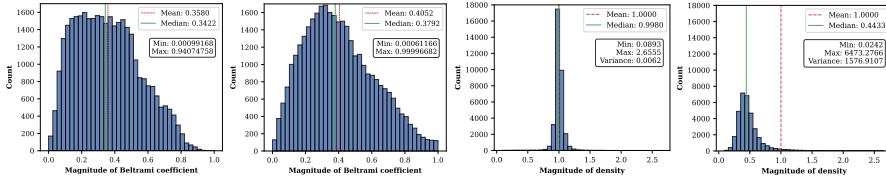


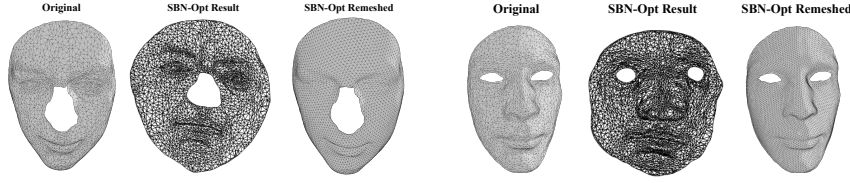
Fig. 11: Quantitative comparison for the "lion face" model against the DEM algorithm. The meaning of each histogram corresponds to that in Fig.9.

with extreme densities; even excluding these, DEM's variance exceeds ours, confirming SBN-Opt's superior global uniformity.

### 9.2.2 Multiply Connected Cases

Our method extends seamlessly to multiply connected domains. The first example is a human face with one hole. In this example, the weights of task loss  $E_1$ , angle distortion loss  $E_{BC}$  and smoothness loss  $E_{smooth}$  are 1, 5e-1 and 1e-4, respectively. Let  $S$  be a surface,  $f : S \rightarrow \mathbb{C}$  be the density-equalizing map, and considering a set of uniformly distributed points  $\mathcal{P}$  on  $f(S)$ , we can triangulate them and obtain a new triangulation  $\mathcal{T}$ . Then, using the inverse mapping  $f^{-1}$ , we can interpolate  $\mathcal{P}$  onto  $S$  and obtain a remeshed triangulation  $(f^{-1}(\mathcal{P}), \mathcal{T})$  of the surface  $S$ . The results are shown in Fig.12a. The average L2 norm of BCs induced by the result mapping is 0.097 and the variance of density is 0.0084.

The second example is a human face with two holes. In this example, the weights of task loss  $E_1$ , angle distortion loss  $E_{BC}$  and smoothness loss  $E_{smooth}$  are 1, 5e-1 and 1e-4, respectively. The results are shown in Fig.12b. The average L2 norm of BCs induced by the result mapping is 0.124 and the variance of density is 0.0127.



(a) Density equalizing parameterization for the human face with one hole. (b) Density equalizing parameterization for the human face with two holes.

Fig. 12: (Left) The original 3D mesh; (Middle) The 2D parameterization result from our SBN-Opt; (Right) The remeshed 3D surface generated from the parameterization derived by SBN-Opt.

### 9.3 Inconsistent surface registration

In this section, we test our SBN-Opt on the problem of inconsistent surface registration. In the application of inconsistent surface registration, our framework demonstrates consistently superior performance when compared to the landmark-dependent LSQC method proposed by Qiu et al [35]. Across three distinct registration tasks, our method achieves mappings with lower angular distortion and improved feature alignment. For details of the problem formulation, see Sec.7.

The first example is the registration of partial tooth surfaces. In Fig.13, the first two columns show the conformal parameterization of the moving surface and the target static tooth surface, respectively. There are 4 regions selected on each surface for alignment and are highlighted in Fig.13. In this example, the weights of intensity matching loss  $E_I$ , landmark matching loss  $E_{pc}$ , angle distortion loss  $E_{BC}$  and smoothness loss  $E_{smooth}$  are 1, 1e-1, 5e-1 and 1e-3, respectively. We compare our result with that of the method in Qiu [35] which is denoted by LSQC in the following. And to perform Qiu’s method, we select four landmarks, one in each region for two surfaces, respectively. As shown in Fig.14, When registering two partial tooth surfaces using four selected feature regions, our method reduced the angular distortion, measured by the average L2 norm of the BCs, by 11.3% (from 0.115 to 0.102). More significantly, the registration accuracy was substantially improved, with the average L1 intensity mismatch error on the overlapping region dropping by 16.9% (from 0.0794 to 0.0660). The registration result in the 2D domain is shown in the third column of Fig.13. The green mesh is the deformed mesh from the source mesh under the bijective deformation map with the blue highlighted regions overlapping orange highlighted regions in the target mesh. The intersection region of the two meshes is the region of correspondence amongst the two tooth surfaces, see Fig.15.

The second example is the registration of two human faces, which are obtained from the FaMoS Dataset [4]. In Fig.16, the first two columns show the conformal parameterization of the moving surface and the target static tooth surface, respectively. There are 4 regions (two eyes, nose and mouth)

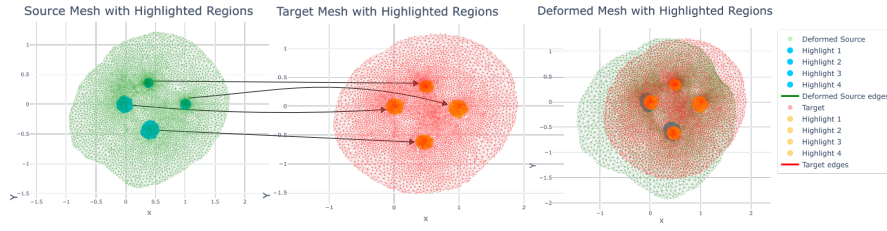


Fig. 13: The first two columns show the conformal parametrizations of the moving and static tooth surfaces, respectively. The region correspondences in the 2D parameter domains are also displayed. The registration result in the 2D domain is shown in the rightmost column.

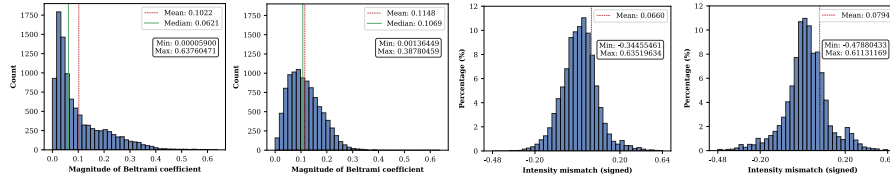


Fig. 14: Statistical comparison of registration results for the tooth surfaces (Fig.13, Fig.15). This figure format is used for all subsequent comparisons (Figs. 17 and 20). The histograms on the left (a, b) compare the angular distortion, measured by the magnitude of the BCs. The histograms on the right (c, d) compare the registration accuracy, measured by the percentage of intensity mismatch error in the overlapping region. In each pair, the result of SBN-Opt is on the left (a, c) and that of the LSQC method is on the right (b, d).

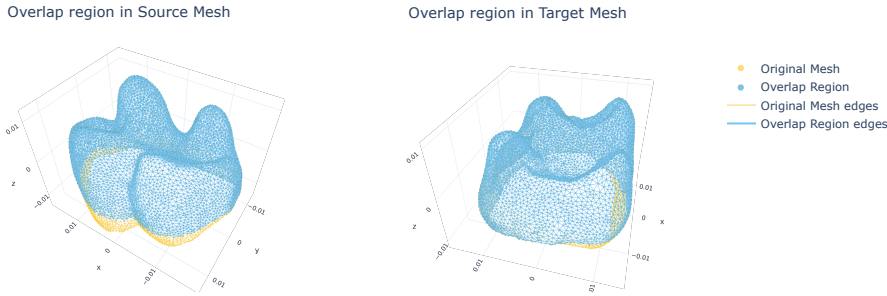


Fig. 15: Visualization of the computed correspondence for the tooth face registration. The identified region of correspondence is highlighted in blue on both the source surface (left) and the target surface (right). The complete surfaces are shown in yellow. This figure illustrates the extensive overlap found by the registration algorithm.

selected on each surface for alignment and are highlighted in Fig.16. And to perform Qiu's method, we select four landmarks, one in each region for two surfaces, respectively. In this example, the weights of intensity matching loss  $E_I$ , landmark matching loss  $E_{pc}$ , angle distortion loss  $E_{BC}$  and smoothness loss  $E_{smooth}$  are 1, 1e-1, 5e-1 and 1e-3, respectively. We compare our result with that of LSQC. As shown in Fig.17, our method yielded even more pronounced



improvements in geometric quality. The average L2 norm of the BCs was reduced by 35.7% (from 0.111 to 0.0711), indicating a much smoother mapping. This was accompanied by a 10.7% decrease in the intensity mismatch error on the overlapping region of correspondence (from 0.0242 to 0.0216). The registration result in the 2D domain is shown in the third column of Fig.16. The green mesh is the deformed mesh from the source mesh under the bijective deformation map with the blue highlighted regions overlapping orange highlighted regions in the target mesh. The intersection region of the two meshes is the region of correspondence amongst the two tooth surfaces, see Fig.18.

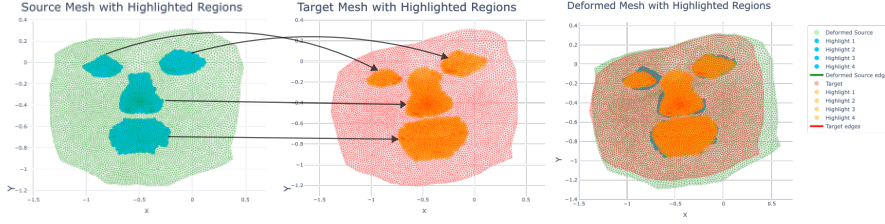


Fig. 16: The first two columns show the conformal parametrizations of the moving and static human faces, respectively. The region correspondences in the 2D parameter domains are also displayed. The registration result in the 2D domain is shown in the rightmost column.

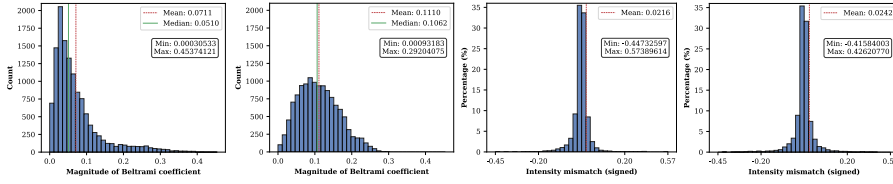


Fig. 17: Quantitative comparison for the full human face registration shown in Fig.16. The meaning of each histogram corresponds to that in Fig.14.

The third case is an example of partial surface registration. Two human faces are cut into two partial faces, both of whose nose and mouth are remained. In Fig.19, the first two columns show the conformal parameterization of the moving surface and the target static tooth surface, respectively. There are 3 regions (bridge of nose, nose and mouth) selected on each surface for alignment and are highlighted in Fig.19. And to perform Qiu's method, we select seven landmarks, two in bridge of nose, three in nose and two in mouth, respectively. In this example, the weights of intensity matching loss  $E_I$ , landmark matching loss  $E_{pc}$ , angle distortion loss  $E_{BC}$  and smoothness loss  $E_{smooth}$  are 1,  $2e-1$ ,  $1e-3$  and  $1e-3$ , respectively. We compare our result with that of LSQC. As shown in Fig.20, our approach demonstrated its most significant advantage



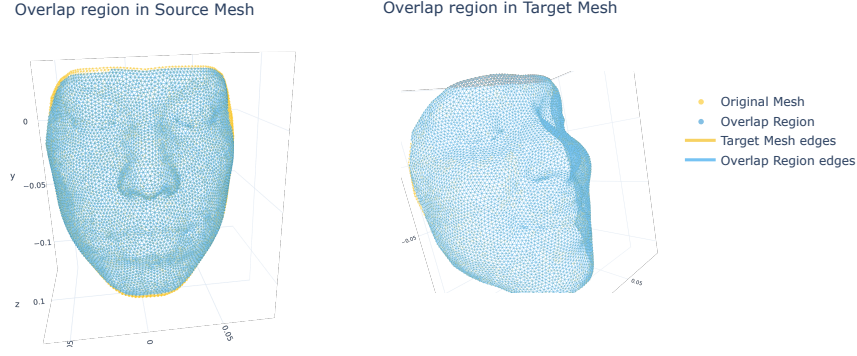


Fig. 18: Visualization of the computed correspondence for the full human face registration.

in reducing distortion. The angular distortion was reduced by an impressive 39.4% (from 0.1464 to 0.0887). The average intensity mismatch error was also reduced by 3.06% (from 0.0327 to 0.0317). Qualitatively, our method produced a more plausible and reasonable correspondence; the resulting overlap region in the source mesh correctly avoided the eye region, an anatomical feature not present in the target partial face. In contrast, the LSQC method produced an overlap that incorrectly extended to the eye region, see Fig.21. The registration result in the 2D domain is shown in the third column of Fig.19. The green mesh is the deformed mesh from the source mesh under the bijective deformation map with the blue highlighted regions overlapping orange highlighted regions in the target mesh.

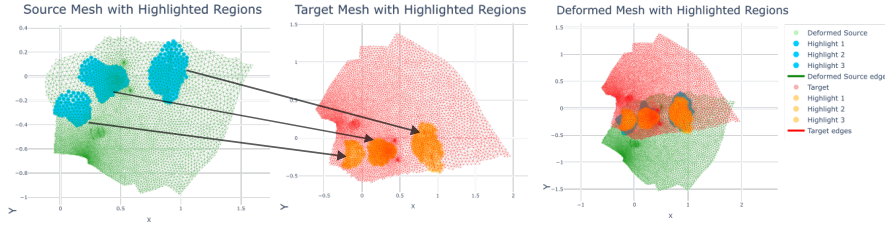


Fig. 19: The first two columns show the conformal parametrizations of the moving and static partial human faces, respectively. The region correspondences in the 2D parameter domains are also displayed. The registration result in the 2D domain is shown in the rightmost column.

## 10 Conclusions

In this work, we introduced SBN-Opt, a novel neural-based framework for free-boundary diffeomorphism optimization, and its core engine, the Spectral

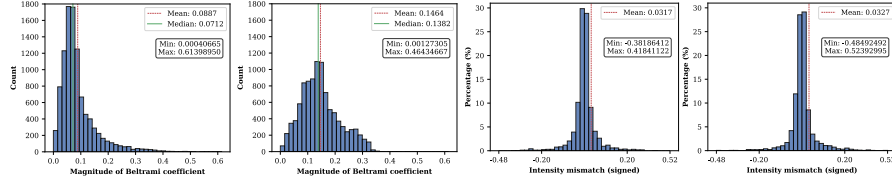


Fig. 20: Quantitative comparison for the partial human face registration shown in Fig.19. The meaning of each histogram corresponds to that in Fig.14.

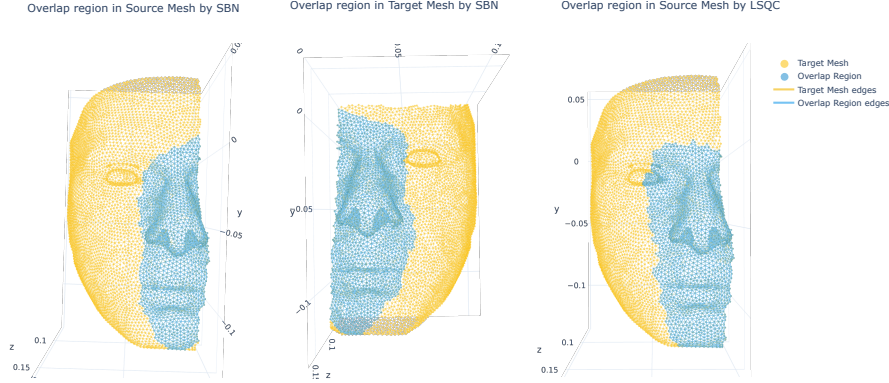


Fig. 21: Visualization of the computed correspondence for the partial human face registration. The identified region of correspondence by our method is highlighted in blue on both the source surface (left) and the target surface (center). The complete surfaces are shown in yellow. Compared with the overlap identified by LSQC on the source mesh (right), computed overlap by our method correctly avoids mapping the eye region of the source, which is not present in the target.

Beltrami Network (SBN). By rigorously establishing the mathematical properties of the Least Squares Quasiconformal (LSQC) energy including existence, uniqueness, similarity-invariance, and resolution-independence, we laid a solid theoretical foundation for SBN-Opt. SBN is a neural surrogate that, for the first time, faithfully approximates the free-boundary LSQC solver. Its unique architecture, which synergistically combines multiscale message-passing with mesh spectral layers, overcomes the limitations of prior methods by effectively capturing both local and global geometric dependencies.

The SBN-Opt framework leverages this powerful surrogate to reframe the complex task of diffeomorphism optimization into a gradient-based problem over the space of BCs and pinned-point conditions. This paradigm shift provides an unprecedented level of explicit control over local geometric distortion while elegantly handling the challenges of free-boundary conditions without the need for artificial constraints or landmark-based scaffolding.

Extensive experiments on density equalization and inconsistent surface registration demonstrate the clear superiority of our approach. SBN-Opt consistently produces mappings with significantly lower distortion and higher accuracy compared to established numerical algorithms. By bridging the gap between the mathematical rigor of quasiconformal geometry and the computational flexibility of deep learning, SBN-Opt provides a powerful, theoretically-grounded, and versatile tool. This work not only addresses long-standing challenges in surface mapping but also paves the way for future advancements in geometry processing, medical imaging, and scientific visualization.

## References

1. Amor, B.B., Arguillere, S., Shao, L.: Resnet-lddmm: advancing the lddmm framework using deep residual networks. *IEEE Transactions on Pattern Analysis and Machine Intelligence* **45**(3), 3707–3720 (2022)
2. Arsigny, V., Commowick, O., Pennec, X., Ayache, N.: A log-euclidean framework for statistics on diffeomorphisms. In: *International Conference on Medical Image Computing and Computer-Assisted Intervention*, pp. 924–931. Springer (2006)
3. Ashburner, J.: A fast diffeomorphic image registration algorithm. *Neuroimage* **38**(1), 95–113 (2007)
4. Bolkart, T., Li, T., Black, M.J.: Instant multi-view head capture through learnable registration. In: *Conference on Computer Vision and Pattern Recognition (CVPR)*, pp. 768–779 (2023)
5. Buchsbaum, B.R., Lemire-Rodger, S., Fang, C., Abdi, H.: The neural basis of vivid memory is patterned on perception. *Journal of cognitive neuroscience* **24**(9), 1867–1883 (2012)
6. Cai, T., Luo, S., Xu, K., He, D., Liu, T.y., Wang, L.: Graphnorm: A principled approach to accelerating graph neural network training. In: *International Conference on Machine Learning*, pp. 1204–1215. PMLR (2021)
7. Chen, Q., Li, Z., Lui, L.M.: A deep learning framework for diffeomorphic mapping problems via quasi-conformal geometry applied to imaging. *SIAM Journal on Imaging Sciences* **17**(1), 501–539 (2024)
8. Choi, G.P., Qiu, D., Lui, L.M.: Shape analysis via inconsistent surface registration. *Proceedings of the Royal Society A* **476**(2242), 20200147 (2020)
9. Choi, G.P., Rycroft, C.H.: Density-equalizing maps for simply connected open surfaces. *SIAM Journal on Imaging Sciences* **11**(2), 1134–1178 (2018)
10. Choi, P.T., Lam, K.C., Lui, L.M.: Flash: Fast landmark aligned spherical harmonic parameterization for genus-0 closed brain surfaces. *SIAM Journal on Imaging Sciences* **8**(1), 67–94 (2015)
11. Choi, P.T., Lui, L.M.: Fast disk conformal parameterization of simply-connected open surfaces. *Journal of Scientific Computing* **65**(3), 1065–1090 (2015)
12. Fortunato, M., Pfaff, T., Wirnsberger, P., Pritzel, A., Battaglia, P.: Multiscale mesh-graphnets. *arXiv preprint arXiv:2210.00612* (2022)
13. Fu, X.M., Liu, Y., Guo, B.: Computing locally injective mappings by advanced mips. *ACM Transactions on Graphics (TOG)* **34**(4), 1–12 (2015)
14. Gardiner, F.P., Lakic, N.: Quasiconformal teichmuller theory. 76. American Mathematical Soc. (2000)
15. Gu, X., Wang, Y., Chan, T.F., Thompson, P.M., Yau, S.T.: Genus zero surface conformal mapping and its application to brain surface mapping. *IEEE transactions on medical imaging* **23**(8), 949–958 (2004)
16. Gu, X., Yau, S.T.: Computing conformal structure of surfaces. *arXiv preprint cs/0212043* (2002)
17. Guo, Y., Chen, Q., Choi, G.P., Lui, L.M.: Automatic landmark detection and registration of brain cortical surfaces via quasi-conformal geometry and convolutional neural networks. *Computers in Biology and Medicine* **163**, 107185 (2023)

18. He, K., Zhang, X., Ren, S., Sun, J.: Deep residual learning for image recognition. In: Proceedings of the IEEE conference on computer vision and pattern recognition, pp. 770–778 (2016)
19. Jin, M., Kim, J., Luo, F., Gu, X.: Discrete surface ricci flow. *IEEE Transactions on Visualization and Computer Graphics* **14**(5), 1030–1043 (2008)
20. Joshi, S.C., Miller, M.I.: Landmark matching via large deformation diffeomorphisms. *IEEE transactions on image processing* **9**(8), 1357–1370 (2000)
21. Kharevych, L., Springborn, B., Schröder, P.: Discrete conformal mappings via circle patterns. *ACM Transactions on Graphics (TOG)* **25**(2), 412–438 (2006)
22. Kovalsky, S.Z., Aigerman, N., Basri, R., Lipman, Y.: Large-scale bounded distortion mappings. *ACM Trans. Graph.* **34**(6), 191–1 (2015)
23. Krebs, J., Delingette, H., Ayache, N., Mansi, T.: Learning a generative motion model from image sequences based on a latent motion matrix. *IEEE Transactions on Medical Imaging* **40**(5), 1405–1416 (2021)
24. Lévy, B., Petitjean, S., Ray, N., Maillot, J.: Least squares conformal maps for automatic texture atlas generation. *ACM Transactions on Graphics* **21**(3), 10–p (2002)
25. Li, Z., Kovachki, N., Azizzadenesheli, K., Liu, B., Bhattacharya, K., Stuart, A., Anandkumar, A.: Fourier neural operator for parametric partial differential equations. *arXiv preprint arXiv:2010.08895* (2020)
26. Loshchilov, I., Hutter, F.: Decoupled weight decay regularization. *arXiv preprint arXiv:1711.05101* (2017)
27. Lui, L.M., Lam, K.C., Wong, T.W., Gu, X.: Texture map and video compression using beltrami representation. *SIAM Journal on Imaging Sciences* **6**(4), 1880–1902 (2013)
28. Lui, L.M., Lam, K.C., Yau, S.T., Gu, X.: Teichmüller mapping (t-map) and its applications to landmark matching registration. *SIAM Journal on Imaging Sciences* **7**(1), 391–426 (2014)
29. Lyu, Z., Choi, G.P., Lui, L.M.: Bijective density-equalizing quasiconformal map for multiply connected open surfaces. *SIAM Journal on Imaging Sciences* **17**(1), 706–755 (2024)
30. Lyu, Z., Lui, L.M., Choi, G.P.: Spherical density-equalizing map for genus-0 closed surfaces. *SIAM Journal on Imaging Sciences* **17**(4), 2110–2141 (2024)
31. Paszke, A.: Pytorch: An imperative style, high-performance deep learning library. *arXiv preprint arXiv:1912.01703* (2019)
32. Persson, P.O., Strang, G.: A simple mesh generator in matlab. *SIAM review* **46**(2), 329–345 (2004)
33. Pietroni, N., Dumery, C., Falque, R., Liu, M., Vidal-Calleja, T.A., Sorkine-Hornung, O.: Computational pattern making from 3d garment models. *ACM Trans. Graph.* **41**(4), 157–1 (2022)
34. Qiu, D., Lam, K.C., Lui, L.M.: Computing quasi-conformal folds. *SIAM Journal on Imaging Sciences* **12**(3), 1392–1424 (2019)
35. Qiu, D., Lui, L.M.: Inconsistent surface registration via optimization of mapping distortions. *Journal of Scientific Computing* **83**, 1–31 (2020)
36. Rabinovich, M., Poranne, R., Panozzo, D., Sorkine-Hornung, O.: Scalable locally injective mappings. *ACM Transactions on Graphics (TOG)* **36**(4), 1 (2017)
37. Russakovsky, O., Deng, J., Su, H., Krause, J., Satheesh, S., Ma, S., Huang, Z., Karpathy, A., Khosla, A., Bernstein, M., et al.: Imagenet large scale visual recognition challenge. *International journal of computer vision* **115**, 211–252 (2015)
38. Smith, J., Schaefer, S.: Bijective parameterization with free boundaries. *ACM Transactions on Graphics (TOG)* **34**(4), 1–9 (2015)
39. Vaswani, A., Shazeer, N., Parmar, N., Uszkoreit, J., Jones, L., Gomez, A.N., Kaiser, L., Polosukhin, I.: Attention is all you need. *Advances in neural information processing systems* **30** (2017)
40. Vercauteren, T., Pennec, X., Perchant, A., Ayache, N.: Diffeomorphic demons: Efficient non-parametric image registration. *NeuroImage* **45**(1), S61–S72 (2009)
41. Wang, J., Zhang, M.: Deepflash: An efficient network for learning-based medical image registration. In: Proceedings of the IEEE/CVF conference on computer vision and pattern recognition, pp. 4444–4452 (2020)
42. Zhu, Z., Choi, G.P., Lui, L.M.: Parallelizable global quasi-conformal parameterization of multiply connected surfaces via partial welding. *SIAM Journal on Imaging Sciences* **15**(4), 1765–1807 (2022)